

Optical and near-IR observations of the faint and fast 2008ha-like supernova 2010ae*

M. D. Stritzinger¹, E. Hsiao², S. Valenti³, F. Taddia⁴, T. J. Rivera-Thorsen⁴, G. Leloudas^{5,6}, K. Maeda^{7,8}, A. Pastorello⁹, M. M. Phillips², G. Pignata¹⁰, E. Baron¹¹, C. R. Burns¹², C. Contreras^{1,2}, G. Folatelli⁷, M. Hamuy¹³, P. Höefflich¹⁴, N. Morrell², J. L. Prieto¹⁵, S. Benetti⁸, A. Campillay², J. B. Haislip¹⁶, A. P. LaClutze¹⁶, J. P. Moore¹⁶, and D. E. Reichart¹⁶

¹ Department of Physics and Astronomy, Aarhus University, Ny Munkegade 120, DK-8000 Aarhus C, Denmark (e-mail: max@phys.au.dk)

² Carnegie Observatories, Las Campanas Observatory, Casilla 601, La Serena, Chile

³ Las Cumbres Observatory Global Telescope Network, Inc. Santa Barbara, CA 93117, USA

⁴ The Oskar Klein Centre, Department of Astronomy, Stockholm University, AlbaNova, 10691 Stockholm, Sweden

⁵ The Oskar Klein Centre, Department of Physics, Stockholm University, AlbaNova, 10691 Stockholm, Sweden

⁶ Dark Cosmology Centre, Niels Bohr Institute, University of Copenhagen, Juliane Maries Vej 30, 2100 Copenhagen Ø, Denmark

⁷ Department of Astronomy, Kyoto University, Kitashirakawa-Oiwake-cho, Sakyo-ku, Kyoto 606-8502, Japan

⁸ Kavli Institute for the Physics and Mathematics of the Universe (IPMU), University of Tokyo, 5-1-5 Kashiwanoha, Kashiwa, Chiba 277-8583, Japan

⁹ INAF-Osservatorio Astronomico di Padova, vicolo dell Osservatorio 5, 35122 Padova, Italy

¹⁰ Departamento Ciencias Físicas, Universidad Andres Bello, Av. Republica 252, Santiago, Chile

¹¹ Homer L. Dodge Department of Physics and Astronomy, University of Oklahoma, 440 W. Brooks, Rm 100, Norman, OK 73019-2061, USA

¹² Observatories of the Carnegie Institution for Science, 813 Santa Barbara St., Pasadena, CA 91101, USA

¹³ Departamento de Astronomía, Universidad de Chile, Casilla 36D, Santiago, Chile

¹⁴ Department of Physics, Florida State University, Tallahassee, FL 32306, USA

¹⁵ Department of Astrophysical Sciences, Princeton University, NJ 08544, USA

¹⁶ University of North Carolina at Chapel Hill, Campus Box 3255, Chapel Hill, NC 27599-3255, USA

Received 22 October 2013 / Accepted 18 November 2013

Abstract

A comprehensive set of optical and near-infrared (NIR) photometry and spectroscopy is presented for the faint and fast 2008ha-like supernova (SN) 2010ae. Contingent on the adopted value of host extinction, SN 2010ae reached a peak brightness of $-13.8 > M_V > -15.3$ mag, while modeling of the UVOIR light curve suggests it produced $0.003\text{--}0.007 M_\odot$ of ^{56}Ni , ejected $0.30\text{--}0.60 M_\odot$ of material, and had an explosion energy of $0.04\text{--}0.30 \times 10^{51}$ erg. The values of these explosion parameters are similar to the peculiar SN 2008ha –for which we also present previously unpublished early phase optical and NIR light curves– and places these two transients at the faint end of the 2002cx-like SN population. Detailed inspection of the post maximum NIR spectroscopic sequence indicates the presence of a multitude of spectral features, which are identified through SYNPPS modeling to be mainly attributed to Co II. Comparison with a collection of published and unpublished NIR spectra of other 2002cx-like SNe, reveals that a Co II footprint is ubiquitous to this subclass of transients, providing a link to Type Ia SNe. A visual-wavelength spectrum of SN 2010ae obtained at +252 days past maximum shows a striking resemblance to a similar epoch spectrum of SN 2002cx. However, subtle differences in the strength and ratio of calcium emission features, as well as diversity among similar epoch spectra of other 2002cx-like SNe indicates a range of physical conditions of the ejecta, highlighting the heterogeneous nature of this peculiar class of transients.

Key words. supernovae: general – supernovae: individual: SN 2008ha, SN 2010ae

1. Introduction

In recent years dedicated transient search programs have led to the tantalizing discovery of a diverse population of hydrogen deficient, rapidly evolving supernovae (SNe). Detailed studies of these new transients have led to the emergence of a hand-

ful of sub-classes whose origins are a matter of open debate. For instance, SNe 2002bj and 2010X had extremely short rise times ($\tau_R \leq 7$ days), reached peak absolute R -band magnitudes (M_R) of -18 and -17 mag, respectively, and exhibited expansion velocities on the order of 10^4 km s^{-1} ; altogether suggestive of progenitors with very small ejected masses, i.e., $< 0.5 M_\odot$ (Poznanski et al. 2010; Kasliwal et al. 2010; Perets et al. 2011). Another group of fast evolving transients recently identified consists of, amongst others, SN 2005E (Perets et al. 2010), PTF 09dav (Sullivan et al. 2011; Kasliwal et al. 2012), and SN 2012hn (Valenti et al. 2013). These objects share the characteristics of low peak luminosities ranging between $M_R \sim -15.5$

* Based on observations collected at the European Organization for Astronomical Research in the Southern Hemisphere, Chile (ESO Program 082.A-0526, 084.D-0719, 088.D-0222, 184.D-1140, and 386.D-0966; the Gemini Observatory, Cerro Pachon, Chile (Gemini Program GS-2010A-Q-14 and GS-2010A-Q-38); the Magellan 6.5 m telescopes at Las Campanas Observatory; and the SOAR telescope.

to -16.5 mag, rapid rise times ($\tau_R \leq 12-15$ days), nebular phase spectra dominated by prevalent calcium features, and are preferentially located in the outskirts of their host galaxies.

Adding to this assortment of newly identified transients are a number of peculiar Type Ia supernovae (SNe Ia) that probably originated from non-standard thermonuclear explosions. Excluding the so-called super-chandrasekhar mass SNe Ia, examples of these typically faint objects that show a diverse set of observational properties include SN 2002es (Ganeshalingam et al. 2012), SNe 2006bt and 2006ot (Foley et al. 2010b; Stritzinger et al. 2011), and PTF10oops (Maguire et al. 2011). In addition to these unusual objects are the members of the spectroscopically defined peculiar 2002cx-like class of SNe Ia, which have recently garnered considerable interest within the community. SN 2002cx-like or Type Iax supernovae (SNe Iax, see Foley et al. 2013, and references therein) exhibit a bizarre set of observational properties including a considerable range in luminosity ($M_R \sim -14$ to -19 mag), as well as low values of kinetic energy ($\sim 10^{49}$ erg) and ejected mass ($0.15-0.5 M_\odot$). Of particular interests is the extreme Type Iax SN 2008ha, which peaks at $M_B \approx -14$ mag and has photospheric expansion velocities between $4500-5500 \text{ km s}^{-1}$, is the faintest and least energetic stripped-envelope SN yet observed (Foley et al. 2009; Valenti et al. 2009; Foley et al. 2010a).

This paper presents detailed optical and near-infrared (NIR) observations of the faint and fast Type Iax SN 2010ae that as we demonstrate, share many characteristics to SN 2008ha. To facilitate a detailed comparison between these two objects, previously unpublished optical and NIR photometry of SN 2008ha taken by the *Carnegie Supernova Project* (CSP; Hamuy et al. 2006) are also presented. To maintain focus on SN 2010ae, details concerning the observations and data reduction of SN 2008ha are deferred to the Appendix. For an in-depth analysis on SN 2008ha the reader is referred to papers by Foley et al. (2009), Valenti et al. (2009), and Foley et al. (2010a).

1.1. Supernova 2010ae

The supernova was discovered in unfiltered images by the Chilean Automatic Supernova sEarch (CHASE; Pignata et al. 2010) on 2010 February 22.06 UT. With J2000.0 coordinates of $\alpha = 07^{\text{h}}15^{\text{m}}54^{\text{s}}.65$ and $\delta = -57^{\circ}20'36''.9$, the location of SN 2010ae is less than $1''.0$ from the center of the type-Sb-peculiar galaxy ESO 162–17 (see Figure 1). Previous non-detection images were obtained on 2010 February 10.11 UT and 2010 February 17.11 UT, indicating that the discovery epoch was within a week after the explosion. To determine the detection limit of these images 1000 artificial stars were distributed randomly within their field, and magnitudes of these stars were computed with the use of the task `SExtractor`. From this exercise a robust 3σ upper detection limit of 19.2 ± 0.1 mag was computed. However, this upper limit is valid only for the field, whereas at the position of the SN the background flux is higher. We then estimated the background noise at the position of the galaxy in the template subtracted pre-discovery search images and compared this to the noise of the field. From this experiment the magnitude limit at the SN position is determined to be 0.33 mag shallower than that of the field. This translates to a final magnitude limit at the position of the SN of 18.9 mag, which is included in the plot of the broadband light curves presented below (see Figure 2).

Based on an initial optical spectrum that exhibited prevalent $\text{C II } \lambda 6580$ absorption, we initially classified SN 2010ae as a bright SN Ia (Stritzinger et al. 2010a). However, with the

addition of spectra covering an extended wavelength range, it became evident this was a low-luminosity 2008ha-like SN Iax around maximum (Stritzinger et al. 2010b). Given its peculiar nature, an intensive followup campaign was initiated, that was made possible through the collaborative efforts between members of the CSP, the *Millennium Center for Supernova Science* (MCSS; Hamuy et al. 2012), and the SN ESO Large Program (PI S. Benetti).

The redshift of ESO 162–17 is listed in the NASA/IPAC Extragalactic Database (NED) as $z = 0.0037$, which when adopting an $H_0 = 73 \pm 5 \text{ km s}^{-1}$, corresponds to a Hubble flow distance (corrected for a Virgo and Great Attractor infall model) of 12.9 ± 0.9 Mpc. This value is consistent with the I -band Tully-Fisher distance of 13.1 ± 3.5 Mpc ($\mu = 30.58 \pm 0.58$ mag) as reported by Springob et al. (2009). In what follows the Tully-Fisher distance is adopted to set the absolute flux scale of SN 2010ae.

2. Host reddening and metallicity estimates

The NED galaxy database provides a Milky Way extinction in the direction of ESO 162–17 of $E(B - V)_{\text{MW}} = 0.124 \pm 0.012$ mag (Schlafly & Finkbeiner 2011), that when adopting a Fitzpatrick (1999) reddening law characterized by an $R_V = 3.1$, corresponds to $A_V = 0.38$ mag.

Accurately estimating the reddening of SN 2010ae associated with dust external to the Milky Way is problematic at best. Unfortunately, the limited sample of SNe Iax currently prevents us from determining whether or not these objects have standard intrinsic colors (Foley et al. 2013). We are therefore largely limited to relying on empirically-derived relations between the equivalent width (EW) of $\text{Na I } D$ absorption and host color excess $E(B - V)_{\text{host}}$. These relations are commonly derived from observations within the Milky Way (e.g. Munari & Zwitter 1997; Poznanski, Prochaska, & Bloom 2012), and provide values with a $\sim 68\%$ uncertainty of the value of A_V (Phillips et al. 2013). Nevertheless, as an initial guide to estimating $E(B - V)_{\text{host}}$ we use this relation based on EW measurements of conspicuous $\text{Na I } D$ contained within the medium-resolution X-shooter spectra (see Section 5.1) at the redshift of the host galaxy. From the series of seven epochs of X-shooter spectra, a Gaussian function was fit to each component, yielding averaged EW values of $\text{Na I } D1 = 0.74 \pm 0.06 \text{ \AA}$ and $\text{Na I } D2 = 0.58 \pm 0.06 \text{ \AA}$. Combining these averaged values with the empirical relation of Poznanski, Prochaska, & Bloom (2012; see their Eq. 9), which provides an approximation between the EW of $\text{Na I } D$ and the color excess within the Milky Way, we obtain $E(B - V)_{\text{host}} = 0.50 \pm 0.42$ mag. Adding this to the Galactic component, the total color excess of SN 2010ae is estimated to be $E(B - V)_{\text{tot}} \sim 0.62 \pm 0.42$ mag (i.e. $A_V = 1.9$ mag). This value is consistent with the $E(B - V)_{\text{tot}} = 0.6$ mag adopted by Foley (2013) for a comparison between a maximum light spectrum of SN 2010ae and the normal Type Ia SN 2011fe. We stress that the application of relations between the EW of $\text{Na I } D$ and color excess are far from quantitative, and provide a rather uncertain estimation. In what follows, results are therefore provided considering a range of dust extinction values extending from the Milky Way component, the combination of the Milky Way and host component derived from the $\text{Na I } D$ absorption, and for the intermediate value $E(B - V)_{\text{moderate}} = 0.30$ mag.

Finally, we note that the Balmer decrement was used to provide another independent measurement of the total color excess. By extracting a region near the position of the SN from our last epoch optical spectrum, $\text{H}\alpha$ to $\text{H}\beta$ line fluxes were measured

to give a ratio of 5.7. Combining this ratio with relations between the Balmer decrement and color excess from Xiao et al. (2012) and Levesque et al. (2010), we obtain total (host+Milky Way) color excess values of $E(B - V)_{tot} = 0.59$ mag and $E(B - V)_{tot} = 0.69$ mag, respectively. These estimates are consistent with the $E(B - V)_{tot} \sim 0.62$ mag inferred from the NaI D absorption. Below broadband color curves are examined as a potential avenue for estimating host extinction (see Section 4.1).

To estimate the metallicity of the host near the location of SN 2010ae, we turn to line diagnostics derived from conspicuous, narrow host-emission features that are readily measured in the low-resolution optical spectra. After careful inspection of the full time series, three epochs of spectra, obtained on 1, 2, and 4 of March 2010 were deemed to be of high enough quality and signal-to-noise to afford robust metallicity measurements.

Oxygen abundance metallicities were derived using the empirically based N2 and O3N2 calibrations of Pettini & Pagel (2004). Gaussian fits to the H α and [N II] $\lambda\lambda 6548, 6583$ emission lines contained within the three epochs yield an averaged local metallicity of $12 + \log(O/H) = 8.40 \pm 0.18$ dex, calibrated on the N2 scale. Here the quoted uncertainty accounts for both measurement and systematic errors. For comparison, the O3N2 method suggests an averaged local metallicity of $12 + \log(O/H) = 8.34 \pm 0.14$ dex, where again the quoted uncertainty includes measurement and systematic errors. These oxygen abundance metallicities correspond to 0.52 and 0.44 the known solar metallicity of ~ 8.69 dex (Asplund et al. 2009), and so are consistent with the metallicity of the LMC.

For comparison, in the case of SN 2008ha, Foley et al. (2009) reported a local metallicity of $12 + \log(O/H) = 8.16 \pm 0.15$ dex, calibrated to the N2 and O3N2 scales. It will be interesting to see in the future if the whole population of SNe Ia occurs in moderately low metallicity environments, or whether this is limited only to those objects located at the extremely faint end of the class.

3. Observations

3.1. Optical and NIR imaging

Two months of $g'r'i'z'BV$ -band and unfiltered imaging of SN 2010ae was performed, extending from -2 to $+61$ days relative to the epoch of B -band maximum (hereafter, $T(B)_{max}$). The broadband monitoring was obtained as a part of CHASE with the PROMPT telescopes (Reichart et al. 2005), while two additional epochs of imaging was taken with the Swope 1-meter (+SITe3 CCD camera) telescope located at the Las Campanas Observatory (LCO). Additionally, starting around maximum and extending for a period of ~ 3 weeks, nine epochs of NIR YJH -band imaging was also obtained at LCO with the Swope 1-m (+RetroCam) and the du Pont (+WIRC) 2.5-m telescopes. All imaging was processed in a standard manner following procedures described in Stritzinger et al. (2011, and reference therein).

Photometry of the SN was computed differentially with respect to a sequence of local stars in the field of the host galaxy. The optical local sequence consists of 22 stars calibrated with respect to Landolt (1992) and Smith et al. (2002) photometric standard fields observed over the course of multiple photometric nights. These standard fields therefore provide $g'r'i'z'$ photometry in the AB photometric system and BV photometry in the Vega photometry system. The NIR local sequence consists of 37 stars calibrated using Persson et al. (1998) standards observed with the Swope, depending on the particular star due to

the pointing of the telescope, over the duration of 2 to 8 photometric nights. The Y -band local sequence was calibrated relative to the $(J - K_s)$ relation provided in Hamuy et al. (2006, see Appendix C, Equation (C2)). Absolute photometry of the local sequence stars is provided in Table 1. We note that our entire sequence of unfiltered images was used to compute an unfiltered light curve relative to the local sequence calibrated to the R band.

Prior to computing photometry of the SN, galaxy subtraction was performed on all science images in order to remove significant contamination associated with host-galaxy light. Multiple optical and NIR templates were obtained with the PROMPT and Swope telescopes well after the SN faded. These images were stacked to create deep master templates and implemented to subtract the galaxy light at the position of the SN following the method described by Contreras et al. (2010).

The light curves of SN 2010ae are plotted in Figure 2, and the corresponding definitive optical and NIR photometry is listed in Tables 2 and 3, respectively. The optical and NIR light curves of SN 2008ha are also plotted in Figure 2 (see Appendix). For comparative purposes the light curves of SN 2008ha have been normalized to match the peak values of SN 2010ae, and are plotted vs. $T(B)_{max}$.

3.2. Spectroscopy

With substantial target-of-opportunity (ToO) access on Gemini-South (+GMOS) and the VLT (+X-Shooter), along with visitor nights at the NTT (+EFOSC, SOFI), SOAR (+GOODMAN), and du Pont (+WFCCD) telescopes, a detailed time series of optical and NIR spectroscopy was obtained for SN 2010ae. The resulting early phase time series consists of 21 spectra covering 20 epochs of optical spectroscopy, extending from -2 d to $+57$ d relative to $T(B)_{max}$, as well as eight NIR spectra covering seven epochs ranging from -1 d to $+18$ d. Additionally, at late phases a visual-wavelength spectrum was taken with the VLT (+FORS2) on $+252$ d. The journal of spectroscopic observations is presented in Table 4.

All low-resolution spectra were reduced in the standard manner using IRAF¹³ scripts following the techniques thoroughly described by Hamuy et al. (2006). To reduce the Gemini-S spectra, we made use of the IRAF `gmos` package following standard reduction methods. In the case of the X-Shooter spectra, the `esorex` pipeline was utilized to produce rectified 2-D images. Each 2-D X-Shooter spectrum was then optimally extracted and flux calibrated using the nightly sensitivity function derived from standard star observations. Telluric absorption corrections derived from observations of appropriate standards obtained prior to and/or after each set of science exposures were applied to each NIR spectrum. When necessary the fluxing of the time series of 1-D spectra was adjusted to match the broadband photometric values. In these instances an average value derived from the ratio between the $g'r'i'z'$ synthetic and broadband magnitudes was applied to the extracted spectra as a multiplicative constant. Since fluxing of the Gemini-S spectra was performed through the use of a generic sensitivity function, the adjustments for these particular spectra were at times as large as a factor of 1.5 of the flux.

¹³ The Image REDuction and Analysis Facility (IRAF) is distributed by the National Optical Astronomy Observatories, which is operated by the Association of Universities of Research in Astronomy, Inc., under cooperative agreement with the National Science Foundation.

The final optical and NIR spectroscopic sequences of SN 2010ae are plotted in Figures 3 and 4, respectively, and the late-phase optical spectrum of SN 2010ae is shown in Figure 12, compared to a similar epoch spectrum of the Type Iax SN 2002cx (Jha et al. 2006).

4. Light Curve Analysis

4.1. Optical and near-IR Light Curves

The photometry of SNe 2008ha and 2010ae plotted in Figure 2 reveal similar bell-shaped light curves, characterized by a fast rise to maximum followed by a subsequent decay, and yield no evidence for a secondary maximum. Basic light curve parameters of these two objects were measured from Gaussian process functional fits to the photometry. Table 5 lists the key observables including the time of maximum, apparent and absolute peak magnitudes, and values of the decline-rate parameter, Δm_{15} . Here Δm_{15} is defined as the magnitude change from the time of maximum brightness to 15 days later. In the case of normal SNe Ia, Δm_{15} is known to correlate with the peak absolute luminosity in such a way that more luminous objects exhibit smaller Δm_{15} values (Phillips 1993). However, in the case of SNe Iax this relationship is known to exhibit significant scatter (Foley et al. 2013). The quoted uncertainty of the light curve fit parameters summarized in Table 5 are robust estimations derived from Monte Carlo simulations, while the associated uncertainty of the absolute magnitudes account for both errors in the fit and the adopted distance. Given our inability to accurately estimate the host extinction, a range in absolute magnitude is given for each passband assuming the Galactic component and $E(B - V)_{tot} = 0.62$ mag. We note that in order to compute the peak absolute magnitudes of SN 2008ha a Galactic reddening value of $E(B - V)_{MW} = 0.07$ mag was used and no host reddening was adopted.

Functional fits to the light curve fits of both SN indicate the following general trends: (i) the bluer the bandpass, the earlier in time maximum light is reached, with a ≈ 9 -day delay between the time of B -band and H -band maxima and, (ii) the bluer the filter, the faster the light curve evolves as parameterized by the decline-rate Δm_{15} .

At peak brightness SNe 2008ha and 2010ae reached $M_B = -13.79 \pm 0.14$ mag and, depending on the adopted extinction value, $-13.44 \pm 0.54 \gtrsim M_B \gtrsim -15.47 \pm 0.54$ mag, respectively. Even when adopting an $A_B = 2.5$ mag, SN 2010ae comfortably sits as the second least luminous SN Iax yet observed, and if only Galactic extinction is adopted, is 0.3 mag less luminous than SN 2008ha. The H -band light curves, which are less susceptible to dust extinction imply SN 2008ha is at most ~ 0.8 mag brighter than SN 2010ae (see Table 5). Interestingly, SN 2010ae exhibits a faster B -band light curve decline with $\Delta m_{15}(B) = 2.43 \pm 0.11$ mag as compared to SN 2008ha with $\Delta m_{15}(B) = 2.03 \pm 0.20$ mag, however, SN 2008ha has marginally higher decline rates in the redder bands (see Table 5).

We now compare optical colors of SNe 2008ha and 2010ae. Color curves normally tend to track the photospheric temperature evolution, and in the case of *some* SN types, can provide constraints on dust extinction. The $(B - V)$, $(V - r)$ and $(V - i)$ color curves of SNe 2008ha and 2010ae are plotted in Figure 5, corrected only for Galactic reddening. For comparison, the $(B - V)$ and $(V - r)$ color curves of the normal Type Ia SN 2006ax (Contreras et al. 2010), are also plotted in Figure 5, and reveal a noticeably different morphology. At the earliest epochs the colors of SNe 2008ha and 2010ae are at their

bluest value, corresponding to the phase when the photospheric temperature is at its highest value. As the ejecta expand and cool the colors evolve towards the red, reaching a maximum value between 15–20 past $T(B)_{max}$, whereupon the colors appear to level off, or in the case of the $(B - V)$ color curve of SN 2008ha evolves back towards the blue.

Comparing the color curves between the two objects, it is evident that at maximum brightness they exhibit nearly identical $(B - V)$ colors, however, by +10d SN 2010ae appears ≈ 0.6 mag redder than SN 2008ha. Interestingly, this is consistent with the estimated upper limit on $E(B - V)_{tot} = 0.62$ mag. However, inspection of the $(V - r)$ and $(V - i)$ colors at the same epoch reveals that SN 2010ae is redder than SN 2008ha by about half of what is expected for $E(B - V)_{tot} = 0.62$ mag. This highlights the complexities of attempting to separate intrinsic colors from effects associated with dust reddening of SNe Iax, and further progress will certainly require an expanded sample to determine if it is at all possible to disentangle these parameters.

4.2. SEDs, UVOIR light curves and light curve modeling

The comprehensive optical and NIR photometry allow for the construction of broadband spectral energy distributions (SEDs) and UVOIR (Ultra-Violet-Optical-InfraRed) bolometric light curves. To begin, the NIR light curves of SNe 2008ha and 2010ae were interpolated so NIR magnitude could be measured on dates corresponding to the optical-band observations. Additionally, the NIR light curves also required extrapolation as their temporal coverage is not as complete as in the optical. This was accomplished by computing the $(i - Y)$, $(Y - J)$, and $(J - H)$ colors at the first and last observed NIR epochs. These colors were then used to extrapolate the NIR light curves to all phases covered by the optical broadband observations. In the case of SN 2008ha its u -band light curve was also extended in time adopting the $(u - B)$ color computed from photometry obtained on the last epoch of u -band observations. Additionally, to extend the time coverage of SN 2008ha’s UVOIR light curves beyond +28d, we utilized published broadband photometry presented by Foley et al. (2009) and Valenti et al. (2009). All of the photometry was next corrected for extinction and converted to flux at the effective wavelength of each passband, allowing for the construction of the SEDs.

Plotted in Figure 6 are the SEDs of SNe 2008ha and 2010ae at maximum light. In the case of SN 2010ae, SEDs are shown for three color excess values. Clearly at this phase (and later) most of the flux is emitted at optical wavelengths, while SN 2010ae shows more flux at red wavelengths than does SN 2008ha. The effect of adopting the high extinction value on the SED of SN 2010ae leads to a larger departure than both the Galactic only extinction value and SN 2008ha. If one were to assume that these two SN have similar intrinsic colors, this would then suggest that the $E(B - V)_{host}$ value based on the EW of NaI D absorption provides an over estimation.

To compute the UVOIR light curves the full time series of SEDs were integrated over flux from B to H bands using a simple trapezoidal technique, and assuming zero flux beyond the extremes of the wavelength range. The results are shown in Figure 7, where for SN 2010ae UVOIR light curves are presented for values of $E(B - V)_{MW} = 0.12$ mag, $E(B - V)_{moderate} = 0.30$ mag, and $E(B - V)_{tot} = 0.62$ mag. Like the individual absolute magnitude light curves, SN 2010ae is found to be, depending on the adopted color excess value, marginally fainter, consistent with or brighter than SN 2008ha.

Key explosion parameters of SNe 2008ha and 2010ae were estimated through model fits to the UVOIR light curves. The model is based on analytical solutions to Arnett's equations (Arnett 1982), and provides estimates of ejecta mass (M_{ej}), the radioactive ^{56}Ni content (M_{Ni}), and the kinetic energy (E_k) of the explosion. The model fits follow the methodology presented by Valenti et al. (2008; see their Appendix A), and relies upon a number of underlying assumptions including: homologous expansion of the ejecta, spherical symmetry, no appreciable mixing of ^{56}Ni , constant optical opacity (in this case $\kappa_{opt} = 0.1 \text{ cm}^2 \text{ g}^{-1}$), and the diffusion approximation for photons. An important input parameter used to compute a model light curve is an expansion velocity (v_{ph}) of the ejecta. We opted to compute a grid of models that encompasses a range of velocities bracketing the value of the photospheric velocity inferred from SYNAPPS (Thomas, Nugent & Meza 2011) synthetic spectral fits to our near maximum light optical spectra of SNe 2008ha and 2010ae (see below). Our SYNAPPS analysis of the near maximum light spectra of SNe 2008ha and 2010ae provides photospheric expansion velocities that range between $4500 < v_{ph} < 5500 \text{ km s}^{-1}$ and $5000 < v_{ph} < 6000 \text{ km s}^{-1}$, respectively.

Final best-fit modeled light curves of SNe 2008ha and 2010ae are plotted as solid lines in Figure 7. The corresponding explosion parameters computed to provide a good match to the UVOIR light curve of SN 2008ha are $M_{Ni} = 0.004 M_{\odot}$, $M_{ej} \sim 0.4\text{--}0.5 M_{\odot}$ and $E_k \sim 0.08\text{--}0.18 \times 10^{51} \text{ erg}$. In the case of SN 2010ae, because of the large uncertainty associated with the host extinction, modeled parameters were derived for each of the UVOIR light curves shown in Figure 7. This analysis provides low, medium, and high adopted extinction modeled parameters of (i) $M_{Ni} = 0.003, 0.004$ and $0.007 M_{\odot}$; (ii) $M_{ej} \sim 0.45\text{--}0.60, 0.35\text{--}0.50$, and $0.30\text{--}0.50 M_{\odot}$; and (iii) $E_k \sim 0.09\text{--}0.30 \times 10^{51}, 0.06\text{--}0.20 \times 10^{51}$, and $0.04\text{--}0.26 \times 10^{51} \text{ erg}$. In summary, when comparing these two faint and fast transients, depending on the adopted host extinction value, we find that SN 2010ae produced a similar amount of M_{Ni} , and marginally higher values of M_{ej} and E_k than SN 2008ha.

5. Spectroscopic analysis

5.1. Early phase spectroscopy

The spectroscopic time series of SN 2010ae (see Figures 3 and 4) represents among the most complete temporal and wavelength coverage yet obtained for an SN Iax, allowing for the opportunity to gain new insight into the nature of this class of transients. The visual-wavelength time series exhibits rich structure characterized by numerous low-velocity P-Cygni spectral features formed by both intermediate-mass elements (IMEs) and Fe-group elements. As the SN evolves through maximum, the strength of many of the IMEs decreases, even becoming in some cases un-identifiable (e.g. C I), while simultaneously, features associated with Fe-group elements begin to dominate. At NIR wavelengths the -1d spectrum exhibits a rather smooth, featureless continuum superposed by a handful of notches. In the next observed spectrum ($+9\text{d}$) a dramatic transformation occurs, revealing a significant number of prominent low-velocity emission features. The spectral evolution is reminiscent of that observed in normal SNe Ia (e.g. Hsiao et al 2013); however, given the extremely low kinetic energy of SN 2010ae, its NIR spectrum exhibits numerous features that emerge relatively rapidly after maximum.

Close examination of the high signal-to-noise spectra of SN 2010ae indicates the presence of a multitude of host-galaxy emission lines associated with a diffuse H II region. Discernible emission features include: [O II] $\lambda 3727$, [Ne III] $\lambda 3969$, [O III] $\lambda \lambda 4959, 5007$, [N II] $\lambda \lambda 6548, 6583$, [S II] $\lambda 6716$, and [Ar III] $\lambda 7136$, as well as Balmer lines at $\lambda \lambda 3835, 3889, 3970, 4102, 4340, 4861, 6563$, and He I $\lambda \lambda 5876, 6678, 7065$ emission features. From a detailed inspection of the 2-D spectra, we can conclude that the extended H II region emission is in the vicinity of the SN; however, the local peak observed in $H\alpha$ is found not to be coincident with the position of the SN.

In addition to the nebular emission lines, an excess of flux blue-wards of $\sim 4500 \text{ \AA}$ is evident in the $+52\text{d}$ and $+248\text{d}$ (see below) spectra, most likely due to incomplete background subtraction. Under closer scrutiny, the absorption features contained within the blue portion of the $+52\text{d}$ spectrum closely resemble those of an E+A post-starburst galaxy. From this we infer that SN 2010ae likely exploded in an environment which underwent an episode of star formation within the last $\sim 1 \text{ Gyr}$.

Returning to the SN features, in order to understand which ions are responsible for the numerous absorption and emission features that characterize the spectroscopic time series of SN 2010ae, we turn to the parameterized spectral synthesis code SYNAPPS (Thomas, Nugent & Meza 2011). Based on the workings of SYNOW (Fisher 2000; Branch, Dang & Baron 2009), SYNAPPS is an enhanced and automated spectral synthesis code that relies on a number of underlying assumptions (for complete details see Thomas, Nugent & Meza 2011, and references therein), and therefore its results should be approached with caution. However, it does provide a fast and effective guide for line identification for a variety of SN types, and is quite useful for studying transient objects that are poorly understood. The input parameters required to compute a synthetic spectrum consist of a black-body temperature (T_{BB}), an e-folding velocity (v_e) for the exponentially declining optical depth distribution, and a list of ions. Each ion requires an additional set of input parameters, including an excitation temperature (T_{exc}), an optical depth (τ), and a photospheric velocity (v_{ph}) of the opacity distribution.

To identify the most pertinent spectral features SYNAPPS models were computed for the -1d and $+18\text{d}$ spectra. Given the lack of absorption features in the -1d NIR spectrum, a fit at this epoch was limited to only optical wavelengths. When computing the SYNAPPS spectrum an extended set of ions was used in the calculation including: C I, C II, O I, Na I, Mg I, Mg II, Si I, Si II, Si III, S I, S II, Ca II, Sc II, Ti II, Cr II, Fe I, Fe II, Fe III, and Co II. The resulting best-fit synthetic spectrum is compared to the -1d spectrum in Figure 8. Here the synthetic spectrum was computed with $v_{ph} = 5960 \text{ km s}^{-1}$, and as indicated in the figure a subset of 12 of the above IMEs and Fe-group ions, which provide plausible contributions to the observed spectral features. Ions of IMEs account for numerous spectral features throughout the optical spectrum, while Fe-group ions are largely responsible for forming a multitude of features that dot the blue end of the spectrum (for a slightly alternative SYNOW spectrum, see Foley 2013).

To obtain a synthetic spectrum that provides a reasonable match to the extended $+18 \text{ day}$ X-Shooter spectrum, it was found that a subset of ions characterized by different v_{ph} values provides the best fits to the observed spectrum. Figure 9 displays the resulting best-fit SYNAPPS synthetic spectrum, where the optical and NIR spectra are shown in the top and bottom panels, respectively. At optical wavelengths a decent synthetic spectrum fit is obtained with $v_{ph} = 4200 \text{ km s}^{-1}$, and the same ions as indicated in Figure 8, except excluding S I, S II and Fe III, and

including Mg II. Instead, the NIR spectrum is found to be described with $v_{ph} = 1700 \text{ km s}^{-1}$, and a smaller subset of ions including O I, Si III, Ca II, Fe II, and Co II. Of these ions, Co II clearly dominates the rich structure observed in the wavelength regions that correspond to the *H* and *K* passbands.

Figure 10 exhibits the time evolution of the blue-shifted line velocities (v_{exp}) for a set of ions that suffer minimal to no line blending. Specifically, v_{exp} is plotted for IMEs and Fe-group ions located at optical wavelengths including Ca II *H&K*, Na I $\lambda 5893$, Si II $\lambda 6355$, C II $\lambda 6580$, Fe II $\lambda 6149$ and Fe II $\lambda 6247$; also plotted are v_{exp} values associated with NIR Co II features at 15759 \AA , 16064 \AA , and 16361 \AA . Around maximum the IMEs exhibit v_{exp} values that range from $\approx 4300 \text{ km s}^{-1}$ up to $\approx 7100 \text{ km s}^{-1}$, while Fe II $\lambda 6149$ exhibits $v_{exp} \approx 6140 \text{ km s}^{-1}$. As the SN evolves, v_{exp} is observed to decrease for all features, with the Fe II $\lambda \lambda 6149, 6247$ features being observed in the +57d spectrum to reach $v_{exp} \sim 1250 \text{ km s}^{-1}$. Between +9d to +18d as the Co II lines emerge and dominate the NIR spectrum their measured line velocities appear consistent with an averaged value ranging from ~ 3300 to 2000 km s^{-1} , which is $\sim 800 \text{ km s}^{-1}$ below those inferred from the optical Fe II features.

5.2. Spectral Comparison of SN 2010ae to relevant SNe Iax

We now proceed to compare spectra of SN 2010ae to other relevant SNe Iax. Plotted in the left panel of Figure 11 are the $-1d$ and $+14d$ visual-wavelength spectra of SN 2010ae compared to similar epoch spectra of SN 2008ha (Foley et al. 2009, 2010a). Overall the comparison reveals that these objects are spectroscopically similar, particularly at maximum. Close inspection indicates that the main difference between these two transients is the blue-shifts of the absorption lines, with SN 2010ae exhibiting higher expansion velocities. This results in an enhancement of line blending of many of the low-velocity spectral features that are more clearly resolved in SN 2008ha (see bottom left panel of Figure 11). Nevertheless, the most prevalent ions in both objects are in close agreement.

Turning our attention to redder wavelengths, unfortunately no NIR spectra of SN 2008ha were obtained preventing a one-to-one comparison. Indeed NIR spectra of the spectroscopic defined SNe Iax class are nearly nonexistent, with the only published observations being those consisting of a sequence of five epochs taken of the bright SN 2005hk (peak $M_V \sim -18$ mag; Phillips et al. 2007), which were recently presented by Kromer et al. (2013). Making use of a subset of that unique data set, plotted in the right panel of Figure 11 is a comparison between NIR spectra of SN 2005hk and SN 2010ae obtained just prior to maximum light and around three weeks later. Interestingly, although SN 2005hk is more than 3 mag brighter than SN 2010ae at maximum, their NIR spectra are very similar. At $-1d$ the spectra are characterized by a relatively smooth continuum with no prevalent features red-wards of $\sim 1.2 \mu\text{m}$. This is consistent with what is observed in other normal SN Ia, however at much earlier epochs (see e.g. Hsiao et al 2013). As revealed in the bottom panel, the +27d spectrum of SN 2005hk exhibits many of the same Fe-group (mostly cobalt) spectral features as in the +18d spectrum of SN 2010ae, though these features become more prominent in SN 2010ae on a shorter timescale.

5.3. Late-phase spectrum

The late-phase spectrum of SN 2010ae provides a unique opportunity to examine the nature of an SN Iax positioned at the faint end of the population. As is evident from Figure 12, the +252d spectrum of SN 2010ae bares a striking resemblance to a similarly aged spectrum of the brighter, prototypical Type Iax SN 2002cx. Like SN 2002cx, the spectrum of SN 2010ae exhibits many low-velocity features associated with both forbidden and P-Cygni permitted Fe II lines (see Jha et al. 2006). The majority of cooling, however, appears to occur through the most prominent emission features being [Ca II] $\lambda \lambda 7291, 7324$, and the Ca II NIR triplet. Additional prevalent features include a P-Cygni line located at $\approx 5870 \text{ \AA}$ that is probably attributed to Na I *D* (however [Co II] $\lambda \lambda 5890, 5908$ cannot be entirely excluded) and forbidden iron lines including [Fe II] $\lambda \lambda 7155, 7453$.

Under close inspection of Figure 12, SN 2010ae does reveal differences with respect to SN 2002cx, the largest being between the [Ca II] and the Ca II NIR triplet emission features, with both exhibiting different line ratios and being significantly more prominent in SN 2010ae. The cause for these differences is probably related to differences in the physical nature of the underlying ejecta. Turning to the analytical work by Li & McCray (1993), we attempt to understand these calcium line differences through the comparison of the allowed temperature vs. number density relation of the underlying ejecta. The adopted relations which were developed under a number of assumptions, including for example that N_e lies within the regime between the critical density of [Ca II] (i.e. $N_e > 10^5 \text{ cm}^{-3}$) and that of the critical density of the Ca II NIR triplet (i.e., $N_e < 10^{11} / \tau_{\text{Ca II}} \sim 10^{8-9} \text{ cm}^{-3}$). In other words, Eq. 21 of Li & McCray (1993), which uses the ratio $([\text{Ca II } \lambda 7291 + \lambda 7324]) / \text{Ca II } \lambda 8542$ as an observational input, is assumed to be roughly valid for N_e values between $10^5 < N_e < 10^9 \text{ cm}^{-3}$. Therefore, by assuming that the ratio of the underlying T_e of the ejecta for both objects is at or near unity, and plugging in the appropriate measured calcium ratios, suggests that the N_e of SN 2010ae is approximately a factor 4 smaller than in SN 2002cx. Alternatively, if the values of N_e for the two objects are fixed to a constant value, this would suggest that the emitting region of SN 2010ae is $\sim 2000 \text{ K}$ less than that of SN 2002cx. We note that these findings are rather insensitive to the range of reddening values that are adopted in this study. From this brief analysis we find that at similar late epochs, the underlying ejecta of SN 2010ae is probably less dense and/or cooler compared to the corresponding line forming regions of SN 2002cx.

Plotted in Figure 13 is the late-phase spectrum of SN 2010ae zoomed in on the wavelength region around the most prominent [Ca II] features, with zero velocity placed at the expected location of [Ni II] $\lambda 7378$. This ion has been associated with a prevalent feature in some SNe Iax (see Foley et al. 2013, their Figure 24), but is clearly not present in SN 2010ae nor in SN 2002cx (see Figure 12). Also indicated in Figure 13 are the expected locations of [Fe II] $\lambda \lambda 7155, 7453$, both of which have been observed in other SNe Iax and core-collapse SNe. The width of the [Ca II] lines is representative of the majority of emission lines that characterize the late-phase spectrum, which exhibit FWHM (Full-Width-Half-Maximum) velocities ranging between ~ 700 to 1000 km s^{-1} , and in addition, show little indication of significant line shifts and/or large scale asymmetries.

In Figure 14 the late-phase spectra of SNe 2002cx and 2010ae are compared to other SNe types at similar epochs. The comparison objects include the normal Type Ia SN 1998bu (Silverman et al. 2013), the under-luminous Type IIP

SN 2008bk, and the Type Ib SN 2007Y (Stritzinger et al. 2009). Overall, the comparison indicates that SNe Iax are in a class of their own. As telling as the spectral features identified in the late-phase spectrum of SN 2010ae may or may not be, equally telling are those features that are not present. For instance the late-phase spectrum of SN 1998bu shown in Figure 14 contains broad emission features associated with the blending of Fe-group features of [Fe III] at ~ 4650 Å, and [Fe II] + [Fe III] at ~ 5300 Å. As ubiquitous as these features are to thermonuclear SNe, they clearly are not evident in the +252d spectrum of SN 2010ae, nor for that matter in all other SNe Iax observed at late phases. Continuing to oxygen, interestingly the spectrum of SN 2010ae shows no evidence for [O I] $\lambda\lambda 6300, 6364$. This feature typically dominates the late-phase spectra in the vast majority of core-collapse SNe (see for example SN 2007Y and to lesser extent SN 2008bk in Figure 14), while it is typically not present in late spectra of thermonuclear SNe Ia (e.g. Blondin et al. 2012; Silverman et al. 2013). Recently, however, [O I] has been observed in the sub-luminous Type Ia SN 2010lp (Taubenberger et al. 2013), and is expected to be observed in turbulent deflagration explosions of C/O white dwarfs, the possible progenitor candidates for bright 2002cx-like SNe Iax (e.g. Phillips et al. 2007; Kromer et al. 2013; Fink et al. 2013).

6. Discussion

The observations presented in this paper confirm the existence of another member of a population of fast evolving, low kinetic energy and low luminosity objects similar to SN 2008ha that have hitherto been missed by transient surveys. To place into context the extreme nature of these faint and fast objects with other SNe, plotted in Figure 15 is a comparison between the peak absolute *B*-band magnitude vs. Δm_{15} for an extended sample of bright, normal and faint SNe Ia observed by the CSP, along with a handful of other well-observed SNe Iax. As confirmed from the figure, SN 2008ha is no longer alone at the extreme end of the luminosity vs. decline-rate relation diagram.

Our model fits to the UVOIR light curves of SNe 2008ha and 2010ae indicates that they have both produced a few $\times 10^{-3} M_{\odot}$ of ^{56}Ni . Although the amount of ^{56}Ni is often correlated with effective temperature of the spectra (Nugent et al. 1997; Höeflich et al. 1996), here we have a low ^{56}Ni mass, which leads to a rapidly receding photosphere. In turn, the effective diffusion time is quite low, and the heating of the ejecta is driven by the decay of ^{56}Ni rather than by ^{56}Co . As ^{56}Ni has a much shorter half-life than ^{56}Co , there is more power available per gram of material (Höeflich et al. 1993). This has the net effect of producing early photospheric spectra that resemble hot and luminous SNe Ia.

Additional insight within the SNe Iax class is provided from our extended observations of SN 2010ae. The detailed NIR spectral time series of SN 2010ae has allowed us to identify a significant number of Fe-group features that we associate predominantly with cobalt. Plotted in Figure 16 is a comparison of post maximum *H*-band NIR spectroscopy of the normal SN 1999ee (Hamuy et al. 2002), the sub-luminous 1991bg-like SN 1999by (Höeflich et al. 2002), and the Type Iax SNe 2005hk (Kromer et al. 2013), 2008ge, 2010ae, and 2012Z. The previously unpublished spectra of SN 2008ge and SN 2012Z were obtained with the VLT equipped with ISAAC (Infrared Spectrometer And Array Camera), and reduced in a standard manner. As discussed earlier in the case of SN 2010ae, a forest of Co II lines dominate this spectral region, and this association evidently holds true for the more luminous Type Iax SN 2008ge (peak $M_V \sim -17.4$

mag; Foley et al. 2010c), SN 2005hk (peak $M_V \sim -18.0$ mag; Phillips et al. 2007), and SN 2012Z (peak $M_V \sim -18.5$ mag; Stritzinger et al., in preparation).

A cobalt footprint appears to be ubiquitous to this class of objects and provides additional confirmation that the faint and fast SN 2010ae is indeed spectroscopically similar to the brighter Type Iax objects like SNe 2002cx and 2005hk. Interestingly, as revealed in the comparison of Figure 16, the structure and distinctiveness of the Co II forest appears to increase as we go down in the plot. This is probably related to the kinetic energy of the explosion with the least energetic objects suffering less line blending effects. The separation of the features depends on the differential expansion rate of the Fe-group element region combined with the wavelength separation of the multiplets. In normal SNe Ia where the differential expansion rate is high, these features are blended leading to the characteristic features observed (Wheeler et al. 1998). However, at longer wavelength ($\sim 2 \mu\text{m}$) the Fe-group element multiplets are only partially blended allowing the individual multiplets to be identified. Even with the large differential expansion rate of normal SNe Ia, the features are reasonable well separated. On the other hand, for sub-luminous 1991bg-like SNe Ia the Fe-group elements are more confined in velocity space, allowing for the identification of individual blended Fe-group multiplets. For SN 2010ae the Fe-group elements are even more confined in velocity space, leading to the well-separated features associated with the individual multiplets.

Although the Type Iax spectral class exhibits some homogeneity there are a number of observational signatures that demonstrate variety, such as that revealed through the comparison of late-phase spectra. We now turn to the presence of [Fe II] $\lambda 7155$ and [Ni II] $\lambda 7378$ emission lines, both of which are thought to be formed in the ashes of a deflagration flame (e.g. Maeda et al. 2010), and thereby provide some clues to the burning physics. Both features are clearly conspicuous in a handful of SNe Iax (Foley et al. 2013). However, through examination of the late-phase spectra of the bright SN 2002cx and now the faint SN 2010ae, we find little to no evidence for [Ni II] $\lambda 7378$ emission, while [Fe II] $\lambda 7155$ is discernible, albeit not at the strength seen in other objects, e.g. SNe 2005P and 2008ge (see Foley et al. 2010c, 2013). A lack of forbidden lines implies high densities consistent with a fast receding photosphere into the high density regions. Additionally, our analysis of the dominant cooling calcium features provides an indication that there are clear differences in the physical conditions of the underlying ejecta. Additional late-phase observations of other low- and high-luminosity SNe Iax are required to determine how cooling is dependent on the physical parameters of the ejecta. Summarizing, the late-phase spectrum of SN 2010ae resembles SN 2002cx; the main differences observed are the strength and line ratios of the calcium features. Finally, we note that all late-phase spectra obtained to date of spectroscopically classified SNe Iax suggest a relative dense ejecta at low velocity (Jha et al. 2006; Foley et al. 2013; McCully et al. 2013), and are substantially different from the spectra of similar aged thermonuclear and core-collapse SNe (see Figure 14).

Initial studies of the bright and energetic Type Iax SNe 2002cx and 2005hk suggested that their observational properties were most consistent with 3-D deflagration models (e.g. Branch et al. 2004; Phillips et al. 2007). Recently, a suite of modeled calculations of Chandrasekhar mass carbon-oxygen white dwarf models that burn via a turbulent deflagration flame and leave a bound remnant has been published (Kromer et al. 2013; Fink et al. 2013; Jordan et al. 2012). These models provide a promising avenue to explain the range of SN Iax luminosities.

ties and explosion energies, however, they appear to produce ^{56}Ni masses that are roughly an order of magnitude larger than the values inferred from the observations of SNe 2008ha and 2010ae. For these extremely low-luminosity, low-ejecta mass objects their origins may be more attuned to the partial thermonuclear incineration of helium-accreting *sub*-Chandrasekhar mass carbon-oxygen white dwarfs that burn via a deflagration flame, and leave a bound remnant (see e.g. Foley et al. 2013). Unfortunately, the viability of this progenitor path remains at best conjecture, and additional modeling efforts including full radiative transfer calculations are required to determine if SN can be simulated that create the low ^{56}Ni masses inferred for the faintest events.

Past efforts to model sub-luminous SNe Ia consist of edge-lit explosions where a helium layer is accreted onto either a sub-Chandrasekhar or a Chandrasekhar mass carbon-oxygen white dwarf, and subsequently initiates a detonation (Livne 1990; Woosley & Weaver 1994; Livne & Arnett 1995) or a double detonation explosion (Fink et al. 2010; Sim et al. 2012; Townsley et al. 2012). Within this realm, even less robust explosions could occur if the edge-lit explosion does not successfully unbind the white dwarf (Bildsten et al. 2007; Shen et al. 2010; Wang et al. 2013a,b). However, it is unclear if any variant within this extended family of models can successfully reproduce all of the most important observables of the least luminous SNe Iax, including low velocities, low ^{56}Ni mass, and the synthesis of IMEs.

Apart from a white dwarf origin others have explored the possibility of fallback models (Valenti et al. 2008; Moriya et al. 2010), as well as electron-capture SNe from super-AGB (Asymptotic Giant Branch) progenitors (Pumo 2010), but these avenues appear less likely given the range of observational properties displayed by the SN Iax class.

Future efforts to model this unique class of stellar explosions will have to consider the broad range of observational details touched on in this study before a consensus can be reached about whether nature prefers a unique or a multiple progenitor path to produce the range of objects that fall under the SNe Iax designation. In a forthcoming paper we will present model calculations for SN 2010ae.

Acknowledgements. Special thanks to the referee who provided a very useful report that improved the quality of this publication. The authors are grateful to R. J. Foley, V. Stanishev and I. R. Seitenzahl for stimulating discussions and providing access to published spectra, as well as to CSP observers L. Boldt, S. Castellon, F. Salgado and W. Krzeminski and staff Astronomers at the Gemini South and ESO VLT observatories for performing observations. M. D. S. and C. C. gratefully acknowledge generous support provided by the Danish Agency for Science and Technology and Innovation realized through a Sapere Aude Level 2 grant. M. D. S., S. V. and F. T. acknowledge funding provided by the Instrument Center for Danish Astrophysics (IDA). M. D. S., K. M. and G. F. acknowledge support by World Premier International Research Center Initiative, MEXT, Japan. G. L. is supported by the Swedish Research Council through grant No. 623-2011-7117. A. P. and S.B. are partially supported by the PRIN-INAF 2011 with the project “Transient Universe: from ESO Large to PESSTO”. G. P. acknowledges funding provided by the Proyecto FONDECYT 11090421. M. H. and G. P. acknowledge support provided by the Millennium Center for Supernova Science through grant P10-064-F (funded by Programa Iniciativa Científica Milenio del Ministerio de Economía, Fomento y Turismo de Chile). This material is also based upon work supported by NSF under grants AST-0306969, AST-0607438 and AST-1008343. This research has made use of the NASA/IPAC Extragalactic Database (NED), which is operated by the Jet Propulsion Laboratory, California Institute of Technology, under contract with the National Aeronautics and Space Administration; as well as resources from the National Energy Research Scientific Computing Center (NERSC), which is supported by the Office of Science of the U.S. Department of Energy under Contract No. DE-AC02-05CH11231.

References

- Arnett, W. D. 1982, *ApJ*, 253, 785
 Asplund, M., Grevesse, N., Sauval, A. J., & Scoot, P. 2009, *ARA&A*, 47, 481
 Bildsten, L., Shen, K., Weinberg, N. N., & Nelemans, G. 2007, *ApJ*, 662, L95
 Blondin, S., Matheson, T., Kirshner, R. P., et al. 2012, *AJ*, 143, 126
 Branch, D., Baron, E., Thomas, R. C., et al. 2004, *PASP*, 116, 903
 Branch, D., Dang, L., & Baron, E. 2009, *PASP*, 121, 238
 Contreras C., Hamuy, M., Phillips, M. M., et al. 2010, *AJ*, 139, 519
 Fink, Röpke, F. K., Hillebrandt, W., et al. A&A, 514, 53
 Fink, M., Kromer, M., Seitenzahl, I., et al., *ArXiv-eprints*, arXiv:1308.3257
 Fisher, A. 2000, Ph.D. thesis, Univ. Oklahoma
 Fitzpatrick, E. L. 1999, *PASP*, 111, 63
 Foley, R. J., Chornock, R., Filippenko, A. V., et al. 2009, *AJ*, 138, 376
 Foley, R. J., Brown, P. J., Rest, A., et al. 2010a, *ApJ*, 708, L61
 Foley, R. J., Narayan, G., Challis, P. J., et al. 2010b, *ApJ*, 708, 1748
 Foley, R. J., Rest, A., Stritzinger, M., et al. 2010c, *AJ*, 140, 1321
 Foley, R. J., Challis, P., Chornock, R., et al. 2013, *ApJ*, 767, 57
 Foley, R. J. 2013, *MNRAS*, 435, 273
 Ganeshalingam, M., Li, W., Filippenko, A. V., et al. 2012, *ApJ*, 751, 142
 Hamuy, M., Maza, J., Pinto, P. A., et al. 2002, *AJ*, 124, 417
 Hamuy, M., Folatelli, G., Morrell, N., & Phillips, M. M. 2006, *PASP*, 118, 2
 Hamuy, M., Pignata, G., Maza, J., Clocchiatti, A., Anderson, J., Bersten, M., Folatelli, G., Forster, F., Gutiérrez, C., Quinn, J., Stritzinger, M., Zelaya, P. 2012, *Mem. Soc. Astron. Italiana*, 83, 388
 Höefflich, P., Mueller, E., & Khokhlov, A. 1993, *A&A*, 268, 570
 Höefflich, P., Khokhlov, A., Wheeler, J. C., et al. 1996, *ApJ*, 427, L81
 Höefflich, P., Gerardy, C. L., Fesen, R. A., Sakai, S. 2002, *ApJ*, 568, 791
 Hsiao, Y. C., Marion, G. H., Phillips, M. M., et al. 2013, *ApJ*, 766, 72
 Jha, S., Branch, D., Chornock, R., et al. 2006, *AJ*, 132, 189
 Jordan I. V., G. C., Perets, H. B., Fisher, R. T., et al. 2012, *ApJ*, 761, L23
 Kasliwal, M. M., Kulkarni, S. R., Gal-Yam, A., et al. 2012, *ApJ*, 723, L98
 Kasliwal, M. M., Kulkarni, S. R., Gal-Yam, A., et al. 2012, *ApJ*, 755, 161
 Landolt, A. U. 1992, *AJ*, 104, 340
 Levesque, E. M., Berger, E., Kewley, L., Bagley, M. M. 2010, *AJ*, 139, L694
 Li, H. W., & McCray, R. 1993, *ApJ*, 405, 730
 Li, W., Filippenko, A. V., Chornock, R., et al. 2003, *PASP*, 115, L453
 Livne, E. 1990, *ApJ*, 354, L53
 Livne, E., & Arnett, D. 1995, *ApJ*, 452, 62
 Kromer, M., Fink, M., Stanishev, V., et al. 2013, *MNRAS*, 429, 2287
 Maeda, K., Benetti, S., Stritzinger, M., et al. 2010, *Nature*, 466, 82
 Maguire, K., Sullivan, M., Thomas, R. C., et al. 2011, *MNRAS*, 418, 747
 McClelland, C. M., Garnavich, P. M., Galbany, L., et al. 2010, *ApJ*, 720, 704
 McCully, C., Jha, S. W., Foley, R. J., et al. 2013, *ArXiv-eprints*, arXiv:1309.4457
 Moriya, T., Tominaga, N., Tanaka, M., et al. 2010, *ApJ*, 719, L1445
 Munari, U., & Zwitter, T. 1997, *MNRAS*, 318, 269
 Nagao, T., Maiolino, R., & Marconi, A. 2006, *A&A*, 459, 85
 Nugent, P., Baron, E., Branch, D., et al. 1997, *ApJ*, 485, 812
 Perets, H. B., Gal-Yam, A., Mazzali, P. A., et al. 2010, *Nature*, 465, 322
 Perets, H. B., Badenes, C., Arcavi, I., et al. 2011, *ApJ*, 730, 89
 Persson, S. E., et al. 1998, *AJ*, 116, 2475
 Pettini, M., & Pagel, B. E. J. 2004, *MNRAS*, 348, 56
 Phillips, M. M. 1993, *ApJ*, 413, L105
 Phillips, M. M., Li, W. D., Frieman, J. A., et al. 2007, *PASP*, 119, 360
 Phillips, M. M., Simon, J. D., Morrell, N., et al. 2013, *ApJ*, 779, 38
 Pignata, G., Cifuentes, M., Maza, J., et al. 2010, *CBET* 2184
 Pilyugin, L. S., & Thuan, T. X. 2005, *ApJ*, 631, 231
 Poznanski, D., et al. 2010, *Science*, 327, 58
 Poznanski, D., Ganeshalingam, M., Silverman, J., Filippenko, A. V. 2011, *MNRAS*, 414L, 81
 Poznanski, D., Prochaska, J. X., & Bloom, J. S. 2012, *MNRAS*, 426, 1465
 Puckett, T., Moore, C., Newton, J., Orff, T. 2010, *CBET* 1567, 1
 Pumo, M. L. 2010, *Mem. S.A.It. Suppl. Vol. 14*, 115
 Reichart, D., et al. 2005, *Nuovo Cimento C*, 28, 767
 Schlafly, E. F., & Finkbeiner, D. P. 2011, *ApJ*, 737, 103
 Schlegel, D. J., Finkbeiner, D. P., & Davis, M. 1998, *ApJ*, 500, 525
 Shen, K. J., Kasen, D., Weinberg, N. N., et al. 2010, *ApJ*, 715, 767
 Silverman, J. M., Ganeshalingam, M., & Filippenko, A. V. 2013, *MNRAS*, 430, 1030
 Sim, S. A., Fink, M., Kromer, M., et al. 2012, *MNRAS*, 420, 3003
 Smith, J. A., Tucker, D., Kent, S., et al. 2002, *AJ*, 123, 2121
 Springob, C. M., Masters, K. L., Haynes, M. P., et al. 2009, *ApJS*, 182, 474
 Stritzinger, M., Mazzali, P., Phillips, M. M., et al. 2009, *ApJ*, 696, 713
 Stritzinger, M., Folatelli, G., Pignata, G., Phillips, M. M. 2010a, *CBET* 2184
 Stritzinger, M., Phillips, M. M., Folatelli, G., Foley, R. J. 2010b, *CBET* 2191
 Stritzinger, M., Phillips, M. M., Boldt, L., et al. 2011, *AJ*, 142, 156
 Sullivan, M., Kasliwal, M. M., Nugent, P., et al. 2011, *ApJ*, 732, 118
 Taubenberger, S., Kromer, M., Pakmor, R., et al. 2013, *ApJ*, 775, L43

- Thomas, R. C., Nugent, P. E., & Meza, J. C. 2011, *PASP*, 123, 237
Townsley, D. M., Moore, K., Bildsten, L. 2012, *ApJ*, 755, 4
Valenti, S., Benetti, S., Cappellaro, E., et al. 2008, *MNRAS*, 383, 1485
Valenti, S., Pastorello, A., Cappellaro, E., et al. 2009, *Nature*, 459, 674
Valenti, S., Yuan, F., Taubenberger, S., et al. 2013, *MNRAS*, ArXiv e-prints, arXiv:1302.2983
Wang, B., Justham, S., & Han, Z. 2013, ArXiv e-prints, arXiv:1301.1047
Wang, B., Justham, S., & Han, Z. 2013, *A&A*, 559, 94
Wheeler, J. C., Hoefflich, P., Harkness, R. P., Spyromilio, J. 1998, *ApJ*, 496, 908
Woosley, S. E., & Weaver, T. A. 1994, *ApJ*, 423, 371
Xiao, T., Wang, T., Wang, H., et al. 2012, *MNRAS*, 421, 486

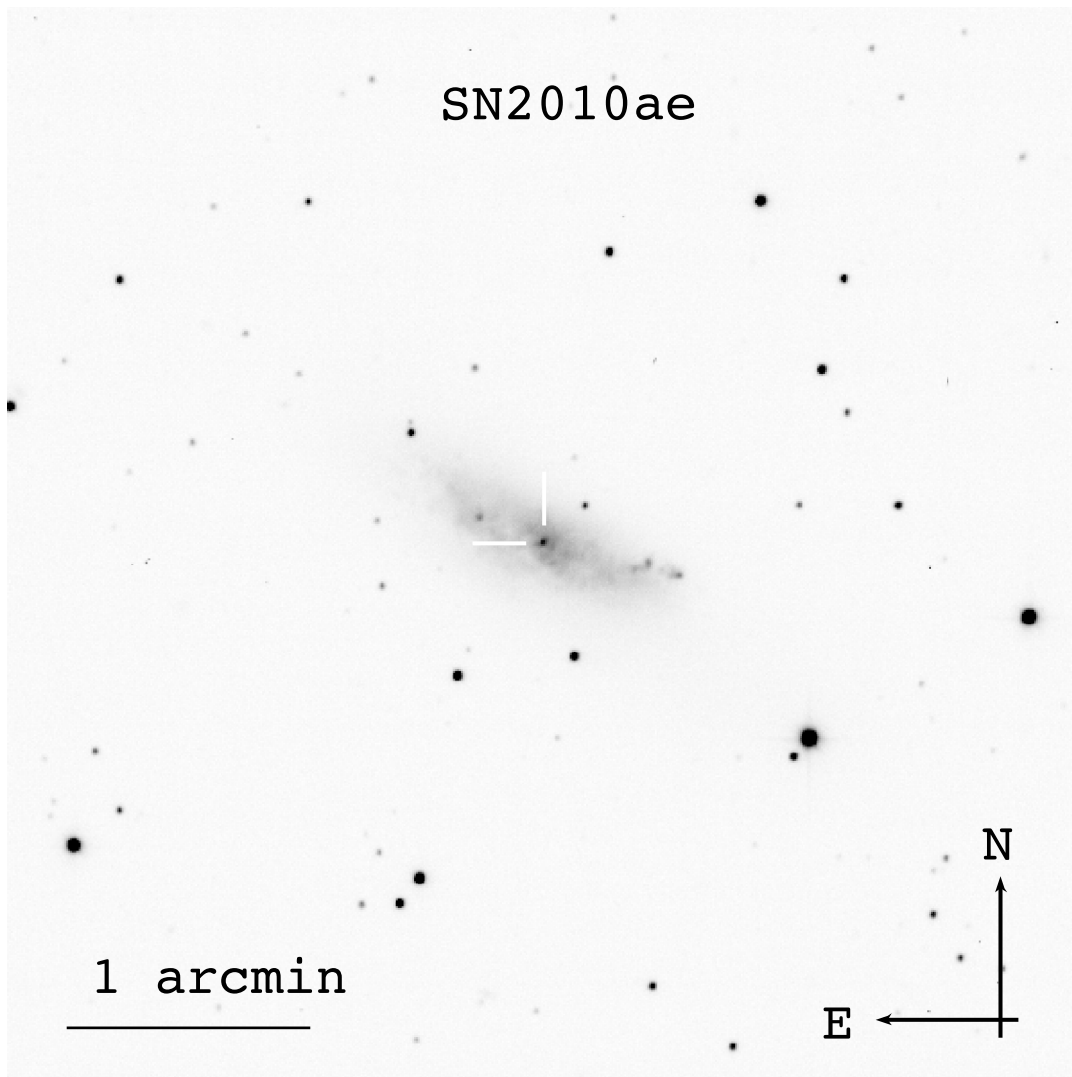


Figure 1: Swope *V*-band image of the Sb-type peculiar galaxy ESO 162–17, with the position of SN 2010ae indicated.

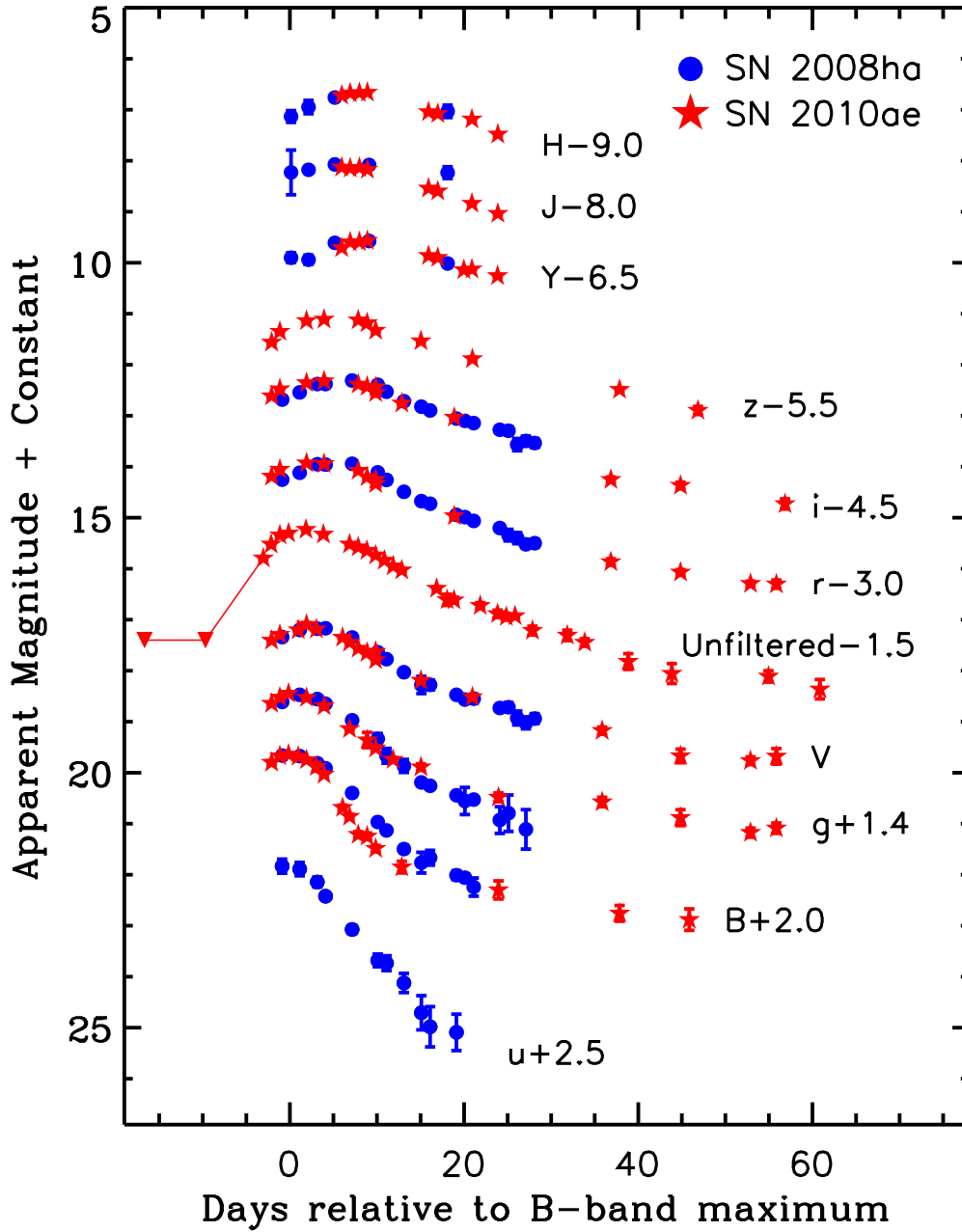


Figure 2: Optical and NIR light curves of SNe 2008ha (blue dots) and 2010ae (red stars) plotted vs. $T(B_{max})$. The light curves of SN 2008ha have been adjusted in apparent magnitude to match the peak values of SN 2010ae. Upside-down red triangles are non-detection upper limits estimated from unfiltered images taken 12 and 5 days prior to discovery.

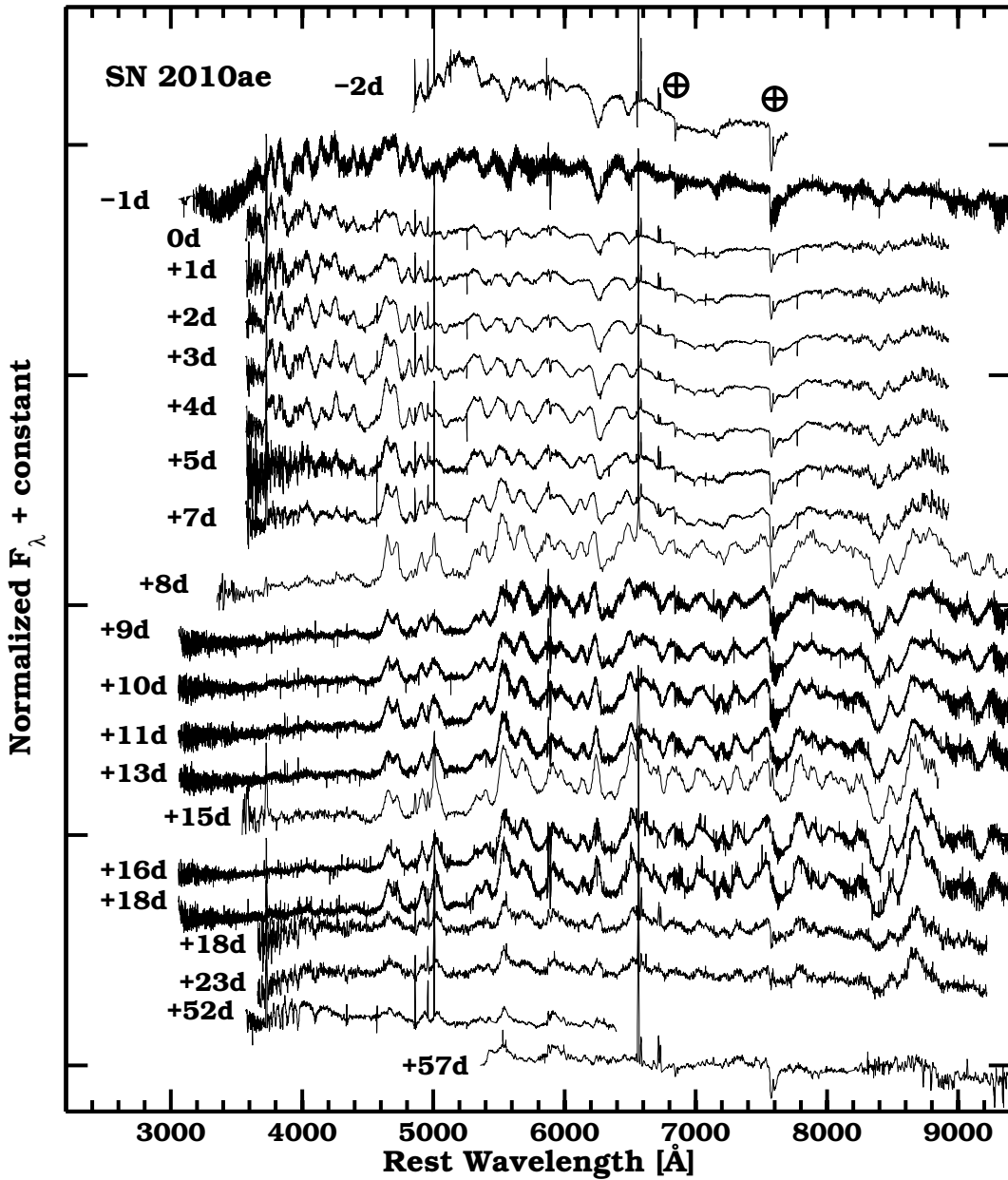


Figure 3: Optical spectroscopic time series of SN 2010ae. Each spectrum has been normalized and corrected to the rest frame of the host galaxy adopting the redshift $z = 0.0037$. The labels on the left indicate the rounded epoch relative to $T(B)_{max}$. We note for clarity each X-Shooter spectrum has been moderately smoothed. Prominent telluric features are indicated with an Earth symbol.

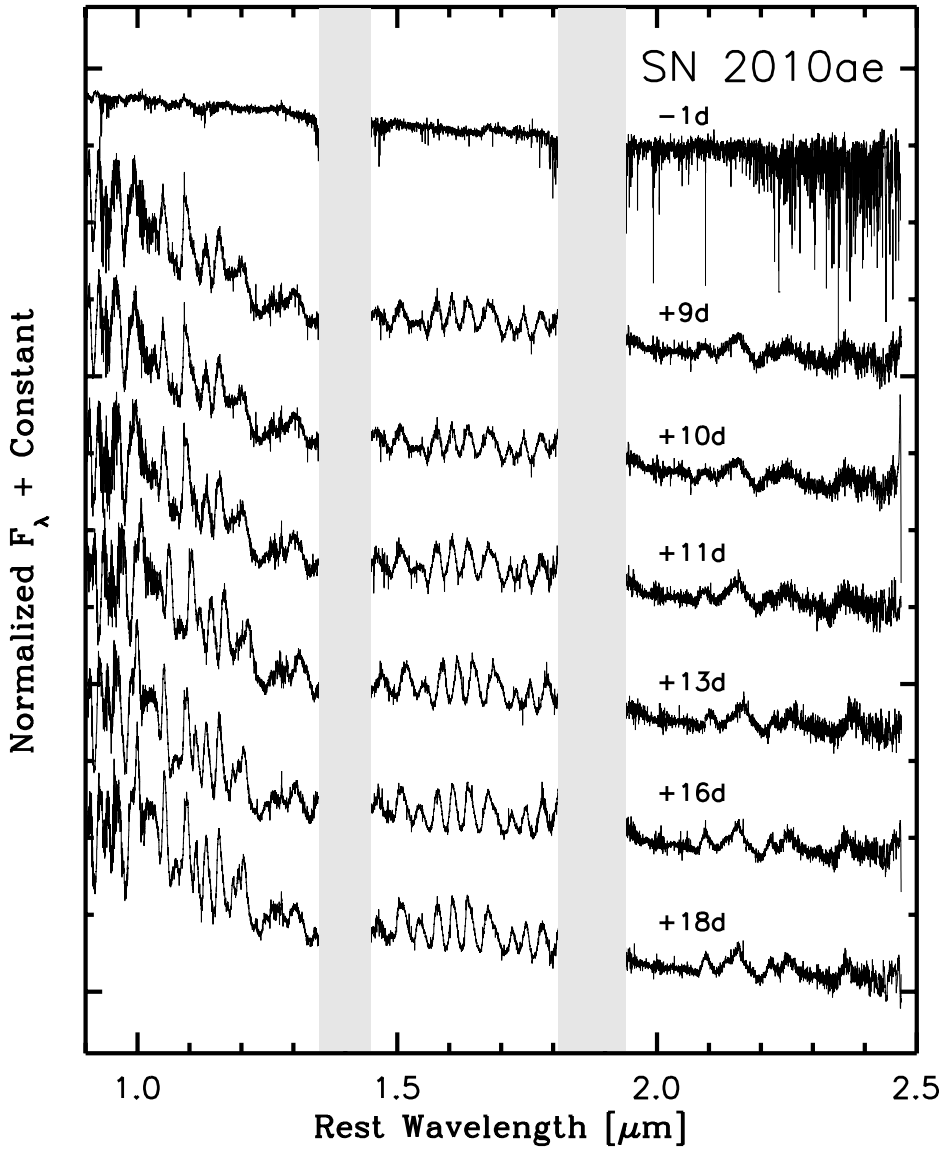


Figure 4: NIR spectroscopy of SN 2010ae taken with the VLT equipped with X-Shooter. Each spectrum has been smoothed, normalized, and corrected to the rest wavelength of the host adopting the redshift $z = 0.0037$. The labels on the right indicate the rounded epoch relative to $T(B)_{max}$. Vertical gray bands mask the most prevalent telluric regions.

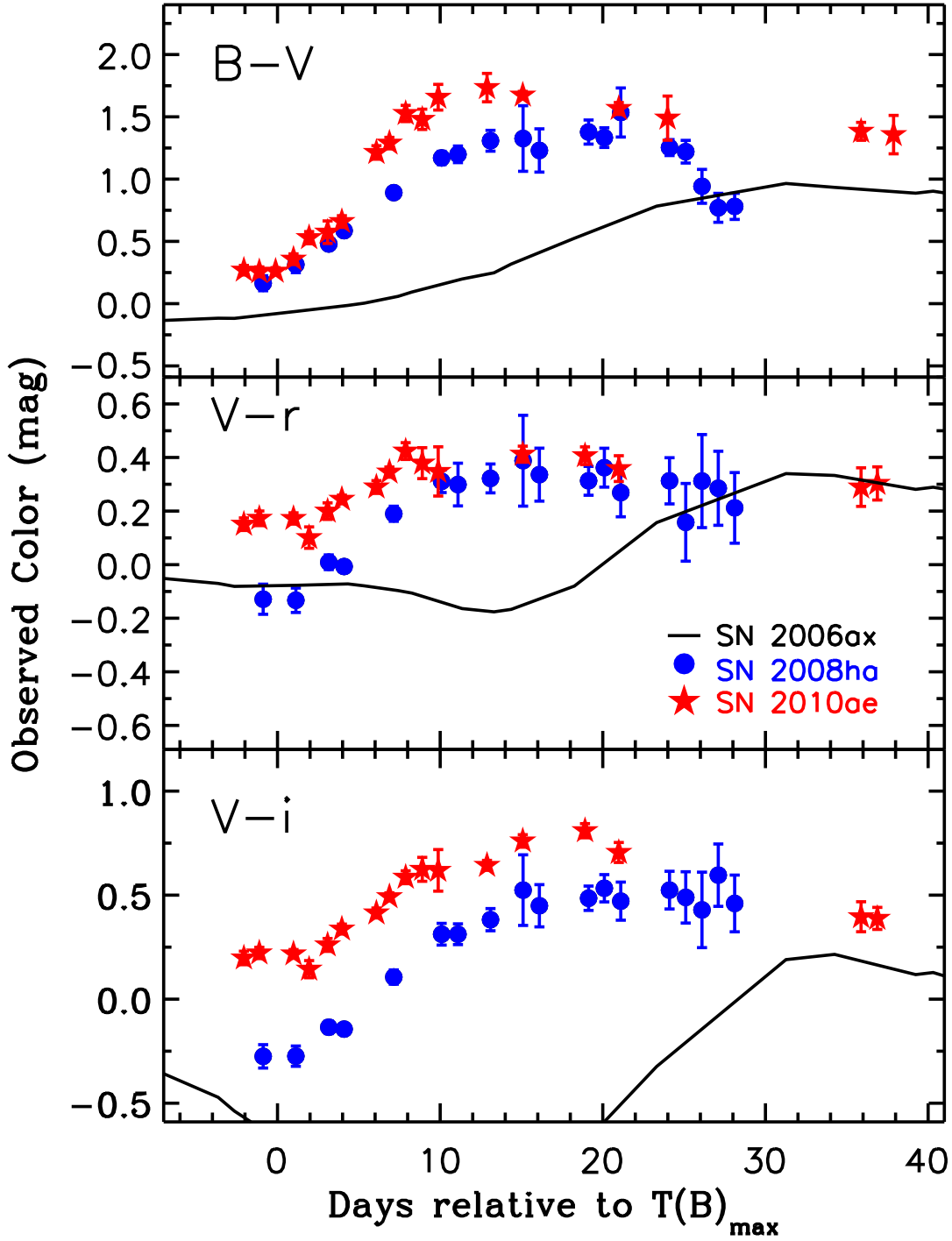


Figure 5: $(B - V)$, $(V - r)$, and $(V - i)$ color curves of the low-luminosity Type Ia SNe 2008ha (blue dots) and 2010ae (red stars), compared to the normal and unreddened Type Ia SN 2006ax (solid line). The color curves have been corrected for Milky Way extinction.

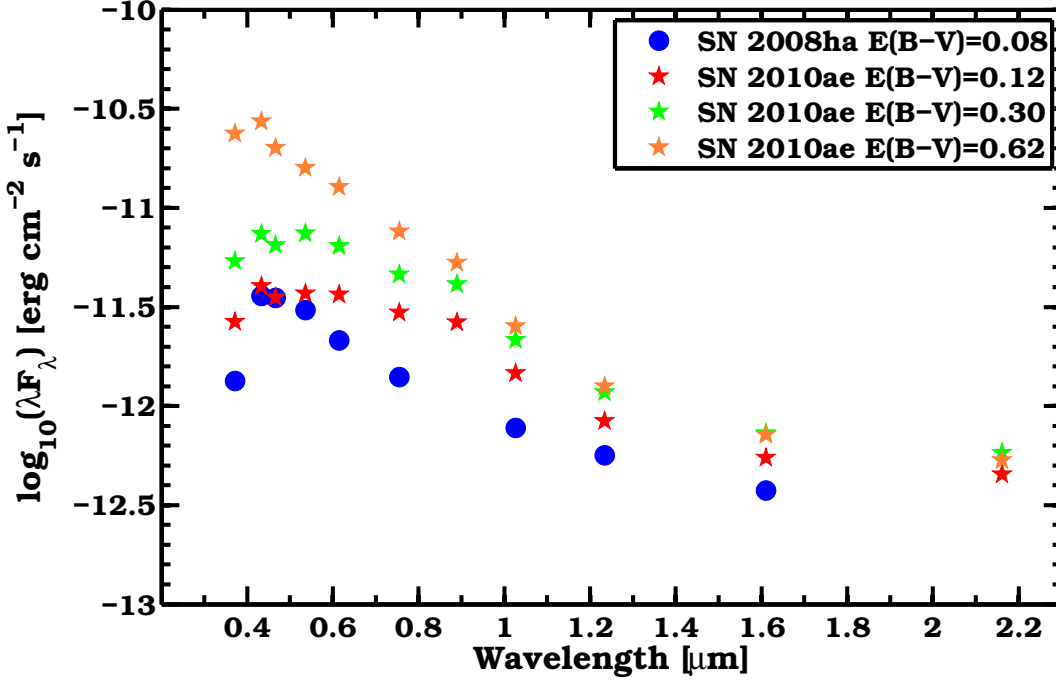


Figure 6: SEDs of SN 2008ha (dots) and SN 2010ae (stars) at maximum light. SEDs of SN 2010ae are plotted for three reddening values, corresponding to the Galactic component (red stars) the combined Galactic plus host component as estimated from the equivalent width of the host’s Na I *D* absorption features, and an intermediate value of these two estimates (see Section 2). The SED of SN 2008ha is constructed from the *u’Bg’Vr’i’YJH* broadband observations corrected for Galactic reddening. The SEDs of SN 2010ae are constructed from measurements obtained with the *Bg’Vr’i’z’YJH* passbands, while the *u’*- and *K_s*-band flux points correspond to measurements provided by the first X-Shooter spectrum.

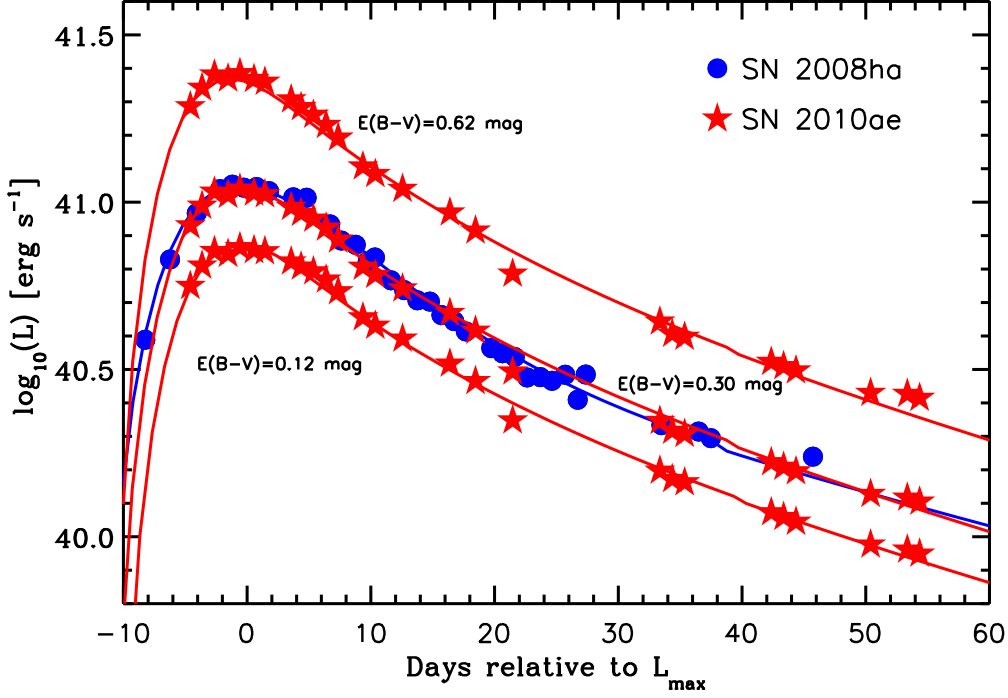


Figure 7: Comparison of the UVOIR light curves of SNe 2008ha and 2010ae. To ensure consistency each UVOIR light curve was constructed through the direct integration of flux between the B and H bands. Given the uncertainty in the reddening estimate of SN 2010ae, UVOIR light curves are plotted assuming $E(B - V)_{\text{MW}} = 0.12$ mag, $E(B - V)_{\text{intermediate}} = 0.30$ mag and $E(B - V)_{\text{tot}} = 0.62$ mag (see Section 2). Over-plotted the UVOIR light curves as solid lines are model fits, from which the values of M_{Ni} , M_{ej} , and E_K are estimated (see Section 4.2).

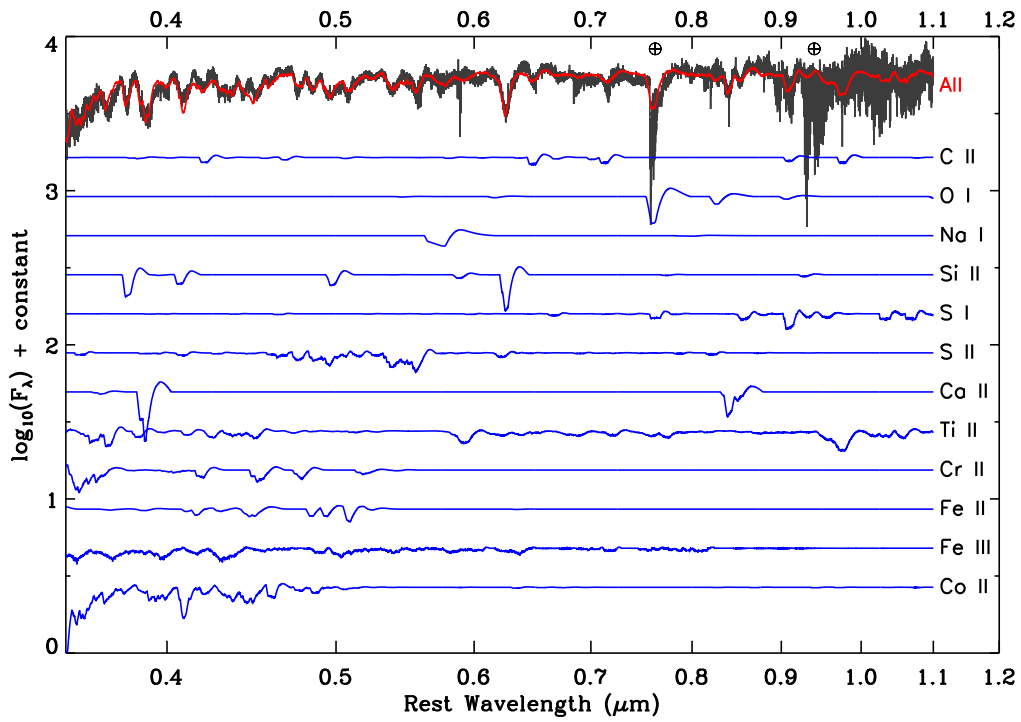


Figure 8: Visual-wavelength $-1d$ X-Shooter spectrum of SN 2010ae (black), compared to the best-fit SYNAPPS synthetic spectrum (red). The various ions included in the model calculations are also plotted. The observed spectrum has been flattened and sigma-clipped. Prevalent telluric regions are indicated with an Earth symbol.

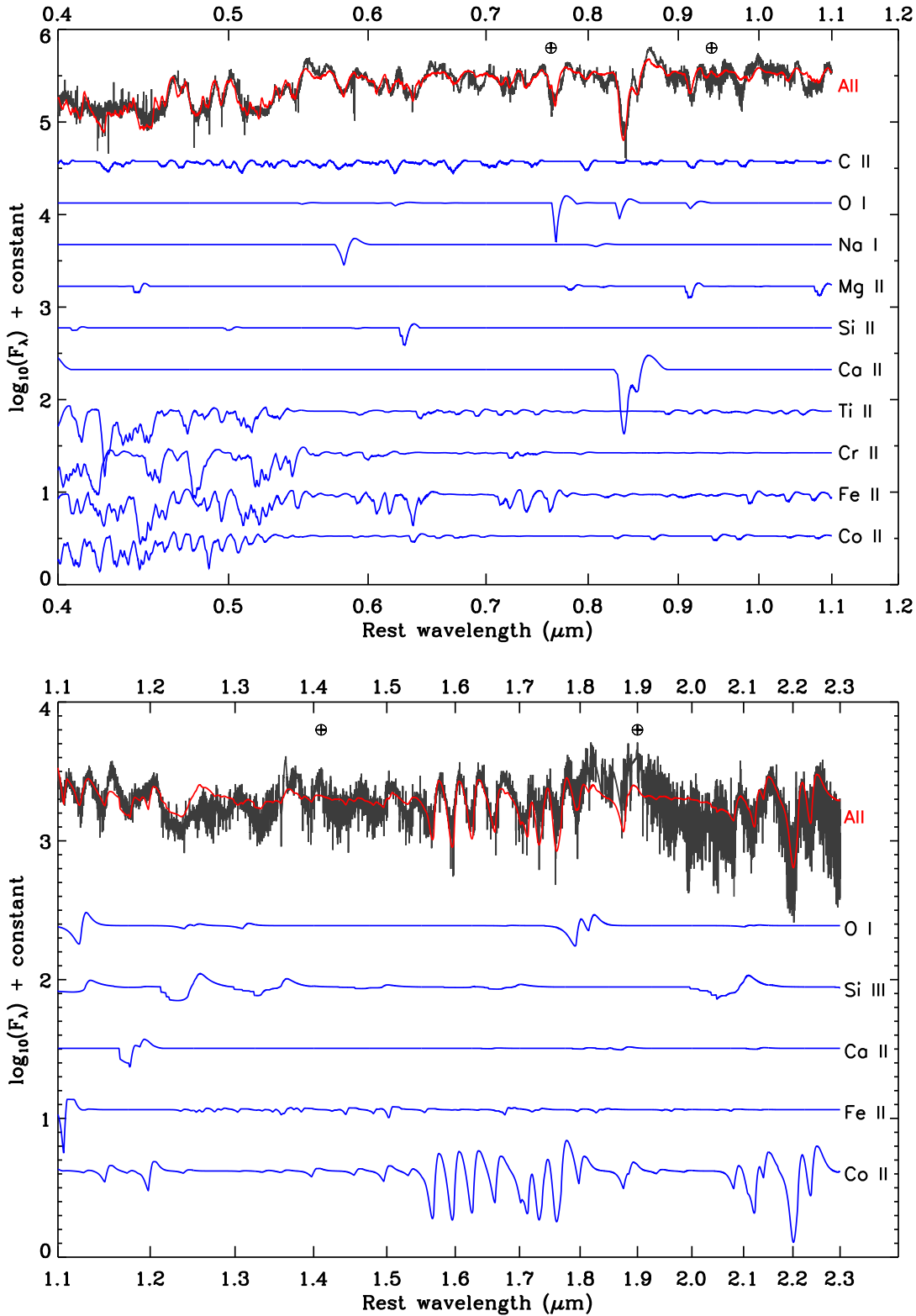


Figure 9: Visual-wavelength (*top*) and NIR (*bottom*): +18d X-Shooter spectrum of SN 2010ae (black), compared to the best-fit SYNAPPS synthetic spectrum (red). The various ions included in the model calculations are also plotted. As discussed in Section 5.1 the synthetic spectra shown here were computed using a different input set of ions and values of v_{phot} . The observed spectrum has been flattened and sigma-clipped. Prevalent telluric regions in the optical are indicated with an Earth symbol.

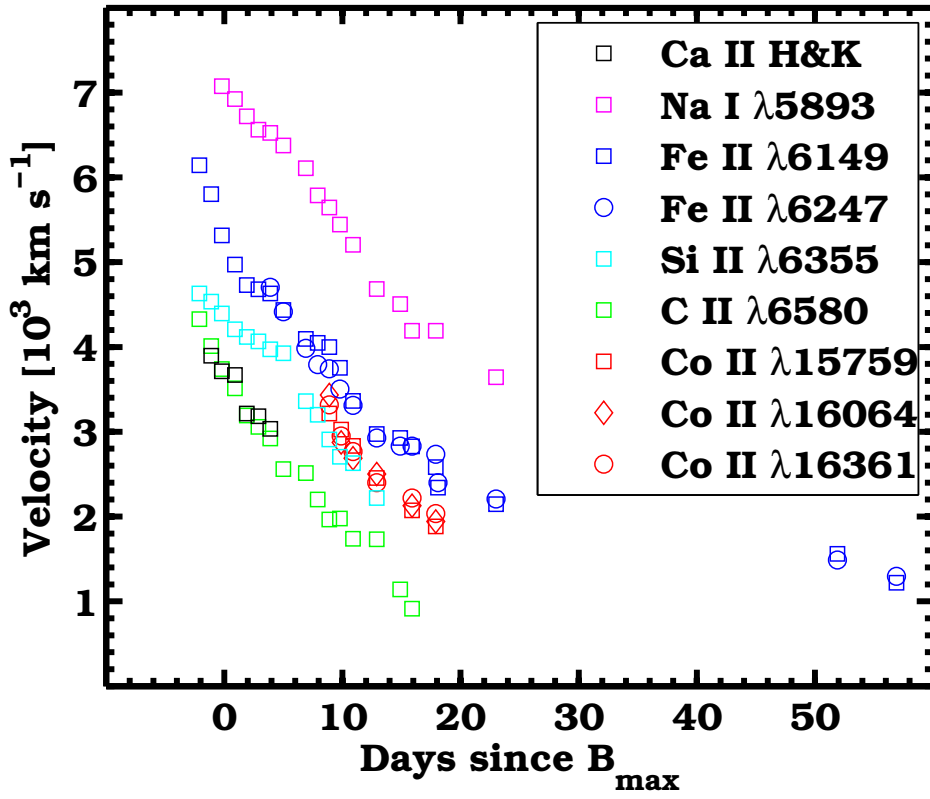


Figure 10: Velocity evolution of the absorption minimum of IMEs and Fe-group spectral features that suffer minimal line blending.

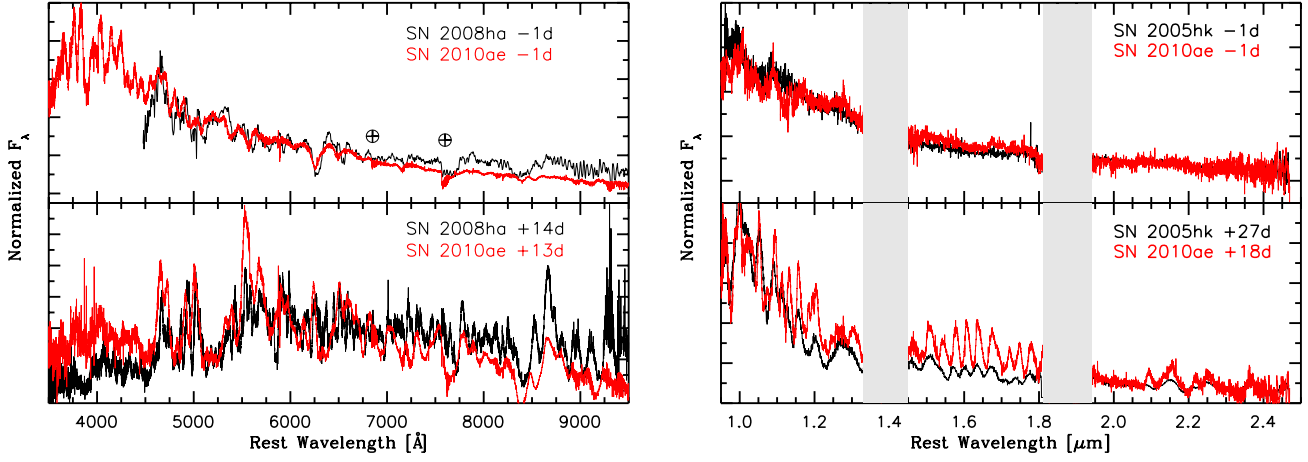


Figure 11: (*left*) Comparison between visual-wavelength spectra of the Type Ia SNe 2008ha (black) and 2010ae (red) taken around maximum light and a fortnight later. The spectra of SNe 2008ha and 2010ae have been corrected to the rest frame adopting redshift values $z = 0.0047$ and $z = 0.0037$, respectively. The spectra of SN 2010ae have also been de-reddened for an $E(B - V)_{tot} = 0.62$ mag. Telluric features are indicated with an Earth symbol. (*right*) Comparison between NIR spectra of the Type Ia SNe 2005hk (black) and 2010ae (red) obtained around maximum light and several weeks later. The spectra of SNe 2005hk and 2010ae have been corrected to the rest frame adopting redshift values $z = 0.0130$ and $z = 0.0037$, respectively. Vertical gray bands mask the most prevalent telluric absorption features.

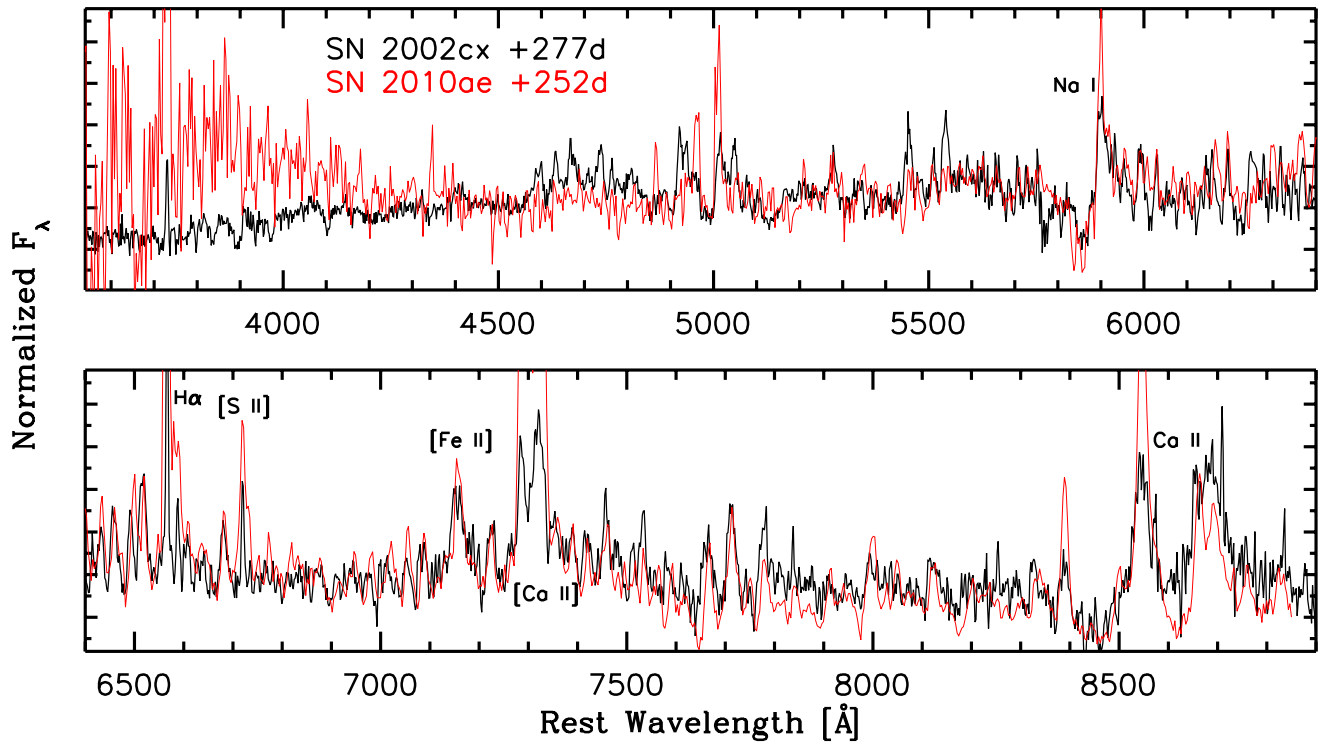


Figure 12: Expanded view of the late-time (+252d) visual-wavelength spectrum of SN 2010ae (red) compared to a similar epoch spectrum (+277d) of the bright Type Iax SN 2002cx (black) (Jha et al. 2006).

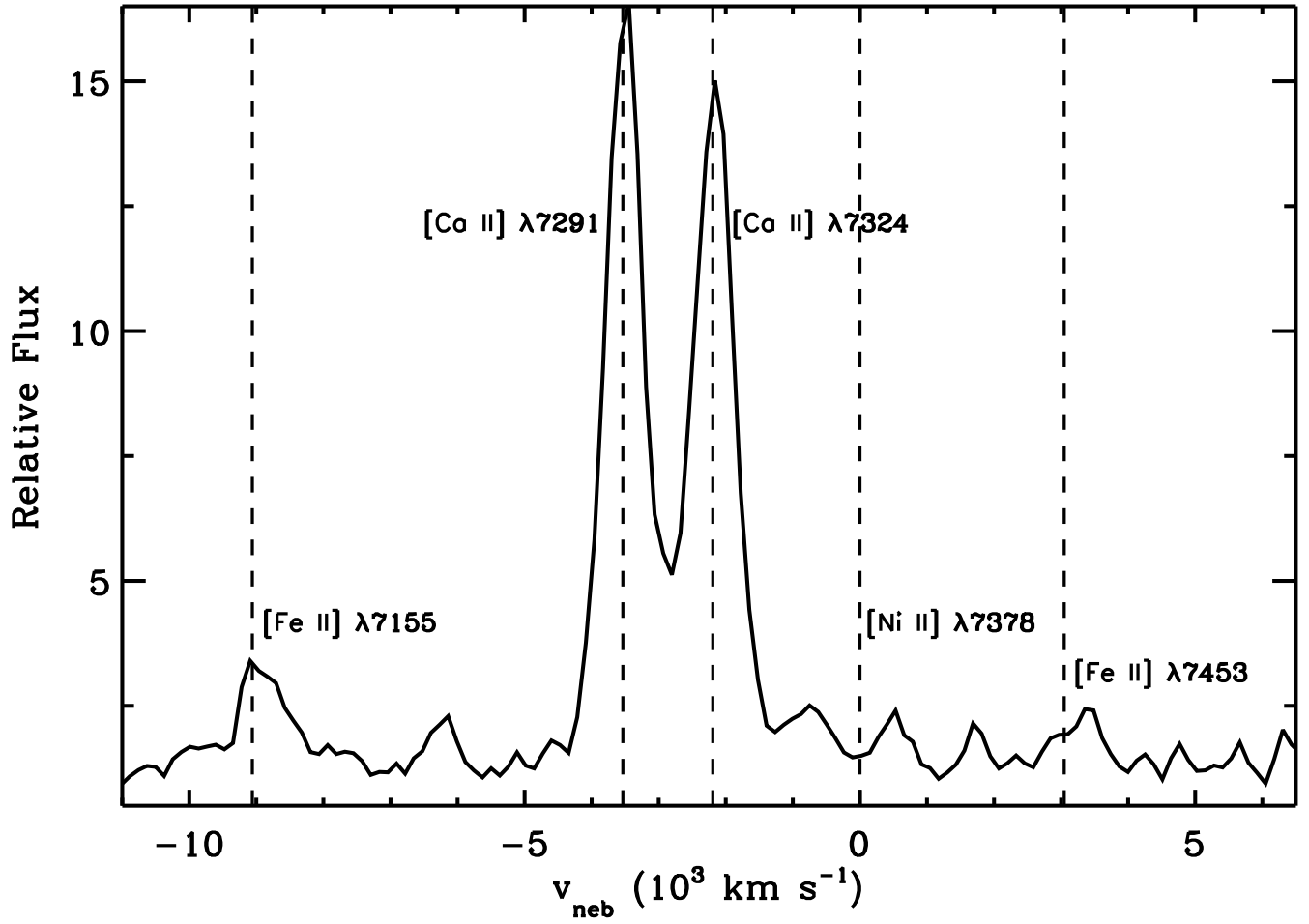


Figure 13: Late-phase spectrum of SN 2010ae centered on the wavelength region around $\sim 7300 \text{ \AA}$.

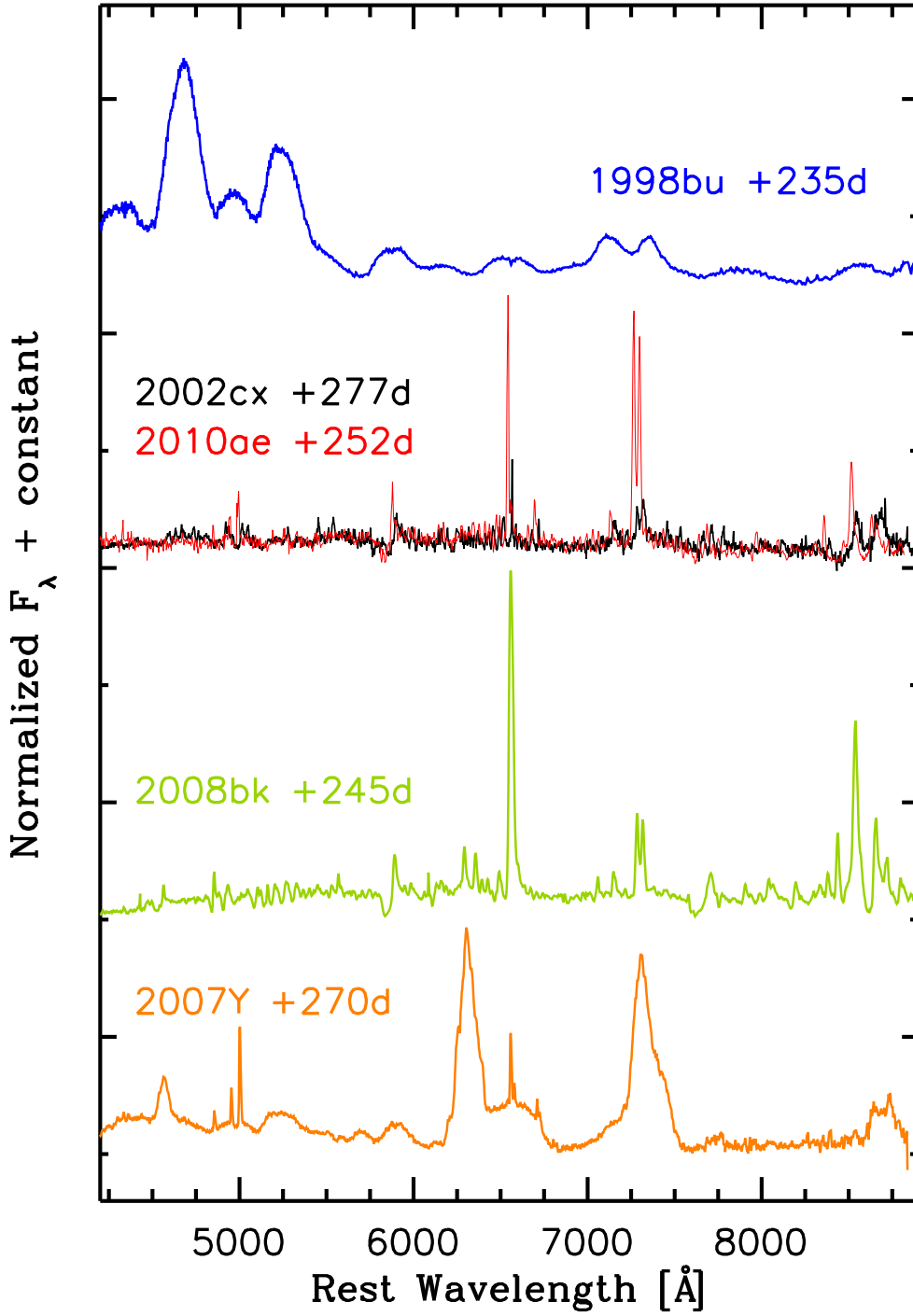


Figure 14: Comparison of the late-phase spectra of the Type Iax SNe 2002cx and 2010ae to similar epoch spectra of the normal Type Ia SN 1998bu (Silverman et al. 2013), the underluminous Type IIP SN 2008bk (CSP, unpublished), and the Type Ib SN 2007Y (Stritzinger et al. 2009). Each spectrum is labeled with respect to $T(B_{max})$, except for SN 2008bk where its epoch is with respect to the date of discovery.

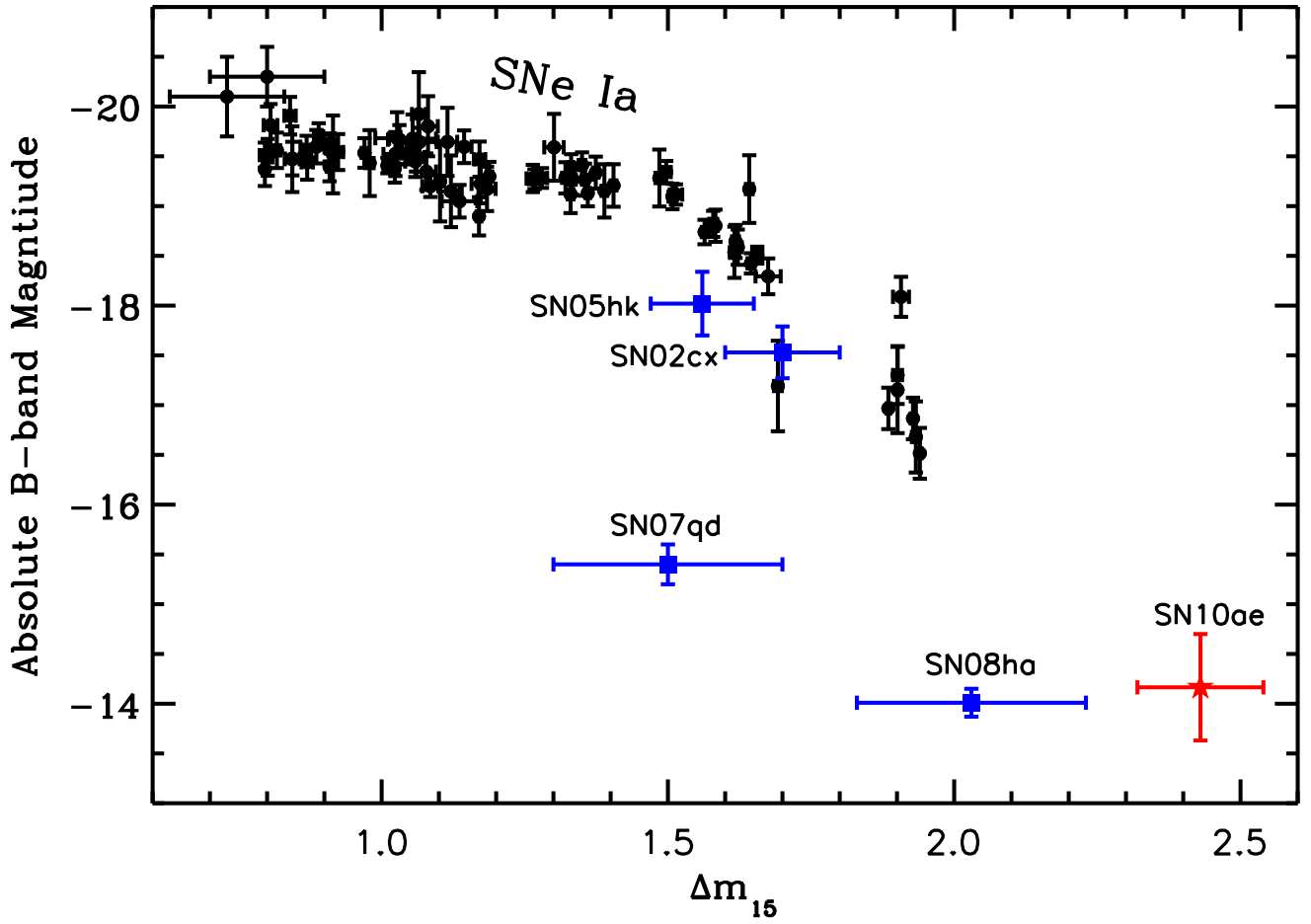


Figure 15: Peak absolute B -band magnitude vs. Δm_{15} for a sample of CSP SNe Ia (black dots), several SNe Iax (blue squares), and SN 2010ae (red star). The SNe Iax plotted from brightest to faintest are SN 2005hk (Phillips et al. 2007), SN 2002cx (Li et al. 2003; Phillips et al. 2007), SN 2007qd (McClelland et al. 2010), and SN 2008ha.

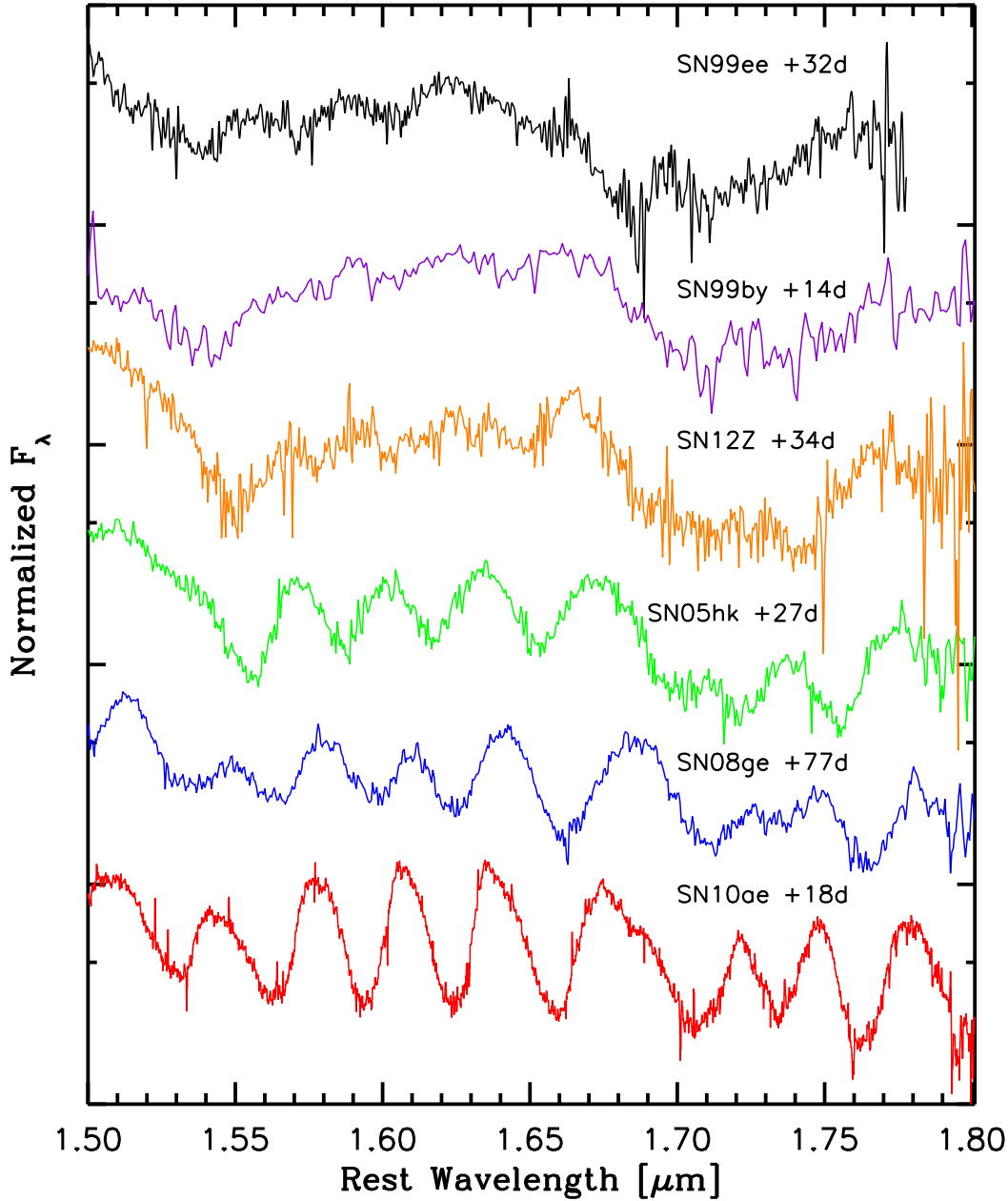


Figure 16: H -band NIR spectroscopy of the normal SN 1999ee (Hamuy et al. 2002) and the sub-luminous Type Ia SN 1999by (Höefflich et al. 2002), compared to the Type Iax SNe 2012Z, 2005hk (Kromer et al. 2013), 2008ge, and 2010ae. The SNe Iax spectra are ordered (top to bottom) from brightest to faintest, and the epoch with respect to maximum light is indicated for each object. CoII features appear to be a ubiquitous signature of SNe Iax class, showing increased prominence in the lowest velocity objects.

Table 1. Optical and NIR photometry of the local sequence of SN 2010ae in the standard system.

STAR	α (2000)	δ (2000)	g' (mag)	r' (mag)	i' (mag)	z' (mag)	B (mag)	V (mag)	R (mag)	Y (mag)	J (mag)	H (mag)
01	07 ^h 15 ^m 50 ^s .15	-57°17'25".12	12.120(026)	11.800(026)	11.692(037)	11.664(019)	12.430(033)	11.941(022)	11.622(016)
02	07 ^h 15 ^m 40 ^s .13	-57°20'55".86	14.282(019)	13.535(020)	13.279(034)	13.148(026)	14.772(018)	13.862(019)	13.307(019)	12.480(009)	12.174(011)	11.726(008)
03	07 ^h 16 ^m 14 ^s .17	-57°20'46".18	15.269(018)	14.415(017)	14.087(033)	13.901(016)	15.863(022)	14.801(021)	14.174(030)	13.206(008)	12.844(010)	12.322(009)
04	07 ^h 16 ^m 08 ^s .86	-57°21'49".82	14.563(026)	14.184(017)	14.045(037)	13.996(012)	14.891(023)	14.351(013)	13.998(012)	13.405(009)	13.189(013)	12.925(008)
05	07 ^h 16 ^m 15 ^s .74	-57°23'03".62	15.463(019)	14.707(027)	14.369(075)	14.179(048)	16.003(024)	15.055(026)	14.493(022)	13.550(009)	13.190(011)	12.680(009)
06	07 ^h 15 ^m 48 ^s .12	-57°19'14".41	15.807(025)	15.172(019)	14.944(027)	14.830(048)	16.249(014)	15.446(025)	14.960(021)	14.193(009)	13.901(014)	13.411(009)
07	07 ^h 16 ^m 01 ^s .29	-57°23'16".08	17.393(765)	16.366(034)	15.470(050)	14.989(053)	18.617(069)	16.999(041)	16.024(011)	14.212(009)	13.765(010)	13.113(009)
08	07 ^h 16 ^m 16 ^s .69	-57°24'28".40	16.732(504)	15.836(014)	15.561(034)	15.382(020)	17.035(029)	16.160(034)	15.592(013)	14.777(014)	14.437(020)	13.964(012)
09	07 ^h 15 ^m 57 ^s .29	-57°21'09".22	16.780(109)	15.798(018)	15.335(041)	15.118(062)	17.435(029)	16.262(026)	15.509(029)	14.351(008)	13.949(012)	13.355(008)
10	07 ^h 15 ^m 47 ^s .91	-57°25'12".47	17.984(044)	16.724(021)	16.039(070)	15.750(066)	12.423(010)	17.347(028)	16.417(028)	14.915(020)	14.483(031)	13.821(012)
11	07 ^h 15 ^m 54 ^s .75	-57°25'03".14	16.710(019)	16.076(031)	15.815(037)	15.681(048)	17.207(038)	16.362(015)	15.864(018)	14.993(020)	14.690(019)	14.258(014)
12	07 ^h 15 ^m 50 ^s .86	-57°23'07".30	15.838(027)	15.376(016)	15.207(031)	15.111(030)	16.202(017)	15.572(022)	15.187(019)	14.518(009)	14.273(011)	13.966(008)
13	07 ^h 15 ^m 49 ^s .86	-57°22'53".26	16.241(025)	15.669(020)	15.451(035)	15.338(033)	16.653(019)	15.922(024)	15.472(016)	14.715(009)	14.436(012)	14.085(009)
14	07 ^h 15 ^m 52 ^s .66	-57°19'26".54	17.420(023)	16.330(033)	15.884(043)	15.649(077)	18.015(024)	16.835(031)	16.045(019)	14.928(008)	14.531(011)	13.925(009)
15	07 ^h 15 ^m 58 ^s .59	-57°22'37".78	20.367(094)	18.862(034)	17.031(061)	16.126(054)	18.276(074)	15.088(008)	14.538(015)	13.996(008)
16	07 ^h 15 ^m 51 ^s .49	-57°22'24".96	18.009(013)	16.801(036)	16.295(018)	15.981(104)	18.647(075)	17.385(019)	16.515(017)	15.207(008)	14.780(009)	14.126(009)
17	07 ^h 16 ^m 07 ^s .36	-57°19'32".66	17.615(013)	16.851(113)	16.468(057)	16.333(067)	18.145(022)	17.181(036)	16.569(027)	15.600(015)	15.244(014)	14.745(009)
18	07 ^h 15 ^m 46 ^s .31	-57°19'55".42	16.934(025)	16.470(039)	16.285(046)	16.220(016)	17.240(022)	16.683(015)	16.291(016)	15.634(009)	15.408(013)	15.060(011)
19	07 ^h 15 ^m 47 ^s .01	-57°20'28".25	19.130(036)	17.863(024)	17.288(069)	16.901(046)	19.672(107)	18.370(048)	17.576(062)	16.131(016)	15.713(013)	15.026(017)
20	07 ^h 16 ^m 12 ^s .81	-57°17'26".92	17.032(026)	16.487(040)	16.313(052)	16.189(054)	17.453(045)	15.628(012)	15.375(017)	15.049(024)
21	07 ^h 16 ^m 01 ^s .68	-57°19'14".02	18.072(028)	17.565(016)	17.383(040)	...	18.391(046)	17.762(046)	17.395(025)	16.659(016)	16.429(028)	16.153(030)
22	07 ^h 16 ^m 09 ^s .04	-57°19'52".21	20.440(142)	19.058(054)	18.180(045)	19.700(114)	18.795(112)	16.811(018)	16.341(026)	15.768(019)
23	07 ^h 16 ^m 20 ^s .30	-57°21'58".14	12.261(008)	11.869(016)	11.304(015)
24	07 ^h 16 ^m 14 ^s .32	-57°21'41".80	13.611(008)	13.376(009)	13.075(009)
25	07 ^h 16 ^m 30 ^s .09	-57°24'21".67	14.252(012)	13.976(036)	13.641(011)
26	07 ^h 16 ^m 09 ^s .64	-57°25'51".38	14.431(014)	14.031(020)	13.540(014)
27	07 ^h 15 ^m 49 ^s .86	-57°25'39".29	15.202(012)	14.899(014)	14.501(014)
28	07 ^h 15 ^m 48 ^s .87	-57°15'59".65	14.006(012)	13.621(020)	13.033(014)
29	07 ^h 16 ^m 16 ^s .80	-57°25'15".24	15.653(012)	15.293(032)	14.789(020)
30	07 ^h 16 ^m 24 ^s .49	-57°20'2".96	15.451(011)	15.142(016)	14.745(017)
31	07 ^h 16 ^m 19 ^s .23	-57°18'47".16	15.609(014)	15.196(018)	14.601(019)
32	07 ^h 16 ^m 07 ^s .36	-57°19'32".66	15.600(015)	15.244(014)	14.745(009)
33	07 ^h 15 ^m 46 ^s .31	-57°19'55".42	15.634(009)	15.408(013)	15.060(011)
34	07 ^h 16 ^m 25 ^s .39	-57°25'49".84	16.201(014)	15.934(026)	15.553(048)
35	07 ^h 16 ^m 26 ^s .31	-57°18'52".20	15.750(010)	15.459(028)	15.039(026)
36	07 ^h 16 ^m 18 ^s .76	-57°16'19".38	14.954(012)	14.653(024)	14.216(017)
37	07 ^h 16 ^m 02 ^s .61	-57°15'48".38	15.060(015)	14.703(020)	14.235(020)
38	07 ^h 16 ^m 26 ^s .50	-57°16'35".62	15.323(012)	15.030(014)	14.632(014)
39	07 ^h 16 ^m 01 ^s .68	-57°19'14".02	16.659(016)	16.429(028)	16.153(030)

Note. — Uncertainties given in parentheses in thousandths of a magnitude correspond to an rms of the magnitudes obtained on photometric nights.

Table 2. PROMPT optical photometry of SN 2010ae in the standard system.

JD−2, 455, 000+	g' (mag)	r' (mag)	i' (mag)	z' (mag)	B (mag)	V (mag)	<i>Unfiltered</i> (mag)
249.6	17.294(036)
250.6	17.643(025)	17.190(015)	17.114(027)	17.061(029)	17.799(034)	17.406(018)	17.021(019)
251.5	17.522(022)	17.054(016)	16.976(016)	16.849(025)	17.672(032)	17.292(022)	16.841(023)
252.5	17.446(020)	17.641(029)	...	16.802(015)
253.6	17.682(037)	17.201(021)	...
254.6	17.529(033)	16.928(019)	16.856(022)	16.639(020)	17.748(034)	17.094(035)	16.732(015)
255.7	17.883(085)	17.185(031)	...
256.6	17.691(042)	16.942(016)	16.820(024)	16.610(018)	18.034(047)	...	16.825(016)
258.7	18.685(049)	17.347(024)	...
259.5	18.139(029)	18.859(042)	17.446(019)	17.019(023)
260.5	...	17.074(016)	16.883(015)	16.624(017)	19.214(059)	17.563(027)	17.075(021)
261.5	18.360(150)	17.200(025)	16.926(025)	16.680(020)	19.248(063)	17.644(052)	17.144(029)
262.5	...	17.253(017)	16.937(017)	...	19.488(062)	17.789(037)	17.234(020)
263.5	18.519(048)	17.334(028)	17.050(067)	16.828(031)	...	17.624(032)	17.338(030)
264.5	18.742(039)	17.448(022)
265.5	17.255(024)	...	19.851(114)	...	17.528(030)
267.7	18.889(063)	17.035(026)	...	18.191(030)	...
269.5	17.887(029)
270.7	18.110(109)
271.5 ^a	...	17.966(033)	17.534(034)	18.116(056)
273.6	17.387(035)	...	18.516(048)	...
274.5	18.224(057)
276.6	19.483(085)	20.298(177)	...	18.384(072)
277.5	18.441(067)
278.5	18.426(032)
280.5	18.712(086)
284.4	18.807(102)
286.5	18.947(074)
288.5	19.575(092)	19.176(072)	...
289.5	...	18.868(062)	18.754(053)
291.5	17.988(039)	20.758(154)	...	19.320(154)
292.5
296.5	19.556(195)
297.5	19.881(157)	19.070(054)	18.869(065)	19.671(133)	...
298.5	20.881(211)
299.5	18.397(079)
305.5 ^a	20.174(089)	19.293(049)
307.6	19.611(111)
308.5	20.088(101)	19.303(081)	19.678(153)	...
309.5	19.230(100)
313.5	19.863(190)

Note. — Values in parentheses are 1σ measurement uncertainties in millimag.

^aPhotometry obtained from Swope images.

Table 3. NIR photometry of SN 2010ae in the standard system.

JD-2, 455, 000+	<i>Y</i> (mag)	<i>J</i> (mag)	<i>H</i> (mag)	Telescope ^a
258.6	16.207(015)	16.128(015)	15.717(015)	DUP
259.6	16.095(015)	16.148(015)	15.674(015)	DUP
260.6	16.092(015)	16.135(015)	15.668(015)	DUP
261.6	16.066(015)	16.171(015)	15.661(015)	DUP
268.6	16.362(015)	16.540(015)	16.043(025)	SWO
269.6	16.400(019)	16.596(015)	16.078(022)	SWO
272.6	16.641(019)	SWO
273.6	16.627(015)	16.837(016)	16.186(032)	SWO
276.5	16.756(024)	17.035(021)	16.481(030)	SWO

Note. — Values in parentheses are 1σ measurement uncertainties in millimag.

^aDUP and SWO correspond to the du Pont and Swope telescopes, respectively.

Table 4. Journal of Spectroscopic Observations.

Date	JD−2,455,000+	Phase ^a	Telescope	Instrument	Grating	Range (Å)	Resolution (FWHM Å)	No. of exposures	Integration (s)
2010 Feb 23	250.57	−2.1	GEM-S	GMOS	R600	4858–7729	8	1	1200
2010 Feb 24	251.51	−1.1	VLT	XSHOOTER	UV+VIS+NIR	3150–24790		8, 8, 16	200, 200, 100
2010 Feb 25	252.52	−0.1	GEM-S	GMOS	B600+R600	3583–8959	8	1, 1	600
2010 Feb 26	253.52	+0.4	GEM-S	GMOS	B600+R600	3583–8959	8	1, 1	600
2010 Feb 27	254.52	+1.9	GEM-S	GMOS	B600+R600	3581–8960	8	1, 1	800
2010 Feb 28	255.51	+2.9	GEM-S	GMOS	B600+R600	3583–8959	8	1, 1	800
2010 Mar 01	256.51	+3.9	GEM-S	GMOS	B600+R600	3583–8959	8	1, 1	800
2010 Mar 02	257.67	+5.0	GEM-S	GMOS	B600+R600	3583–8959	8	1, 1	850
2010 Mar 04	259.57	+6.9	GEM-S	GMOS	B600+R600	3582–8959	8	1, 1	700
2010 Mar 05	260.52	+7.9	NTT	EFOSC	gm#11+gm#16	3352–10291	14	1, 1	600
2010 Mar 06	261.55	+8.9	VLT	XSHOOTER	UV+VIS+NIR	3150–24790	0.8, 0.8, 3.2	4, 4, 8	600, 600, 300
2010 Mar 07	262.51	+9.9	VLT	XSHOOTER	UV+VIS+NIR	3150–24790	0.8, 0.8, 3.2	4, 4, 8	600, 600, 300
2010 Mar 08	263.52	+10.9	NTT	SOFI	GB+GR	9358–25000	27, 30	12, 20	120
2010 Mar 08	263.55	+10.9	VLT	XSHOOTER	UV+VIS+NIR	3150–24790	0.8, 0.8, 3.2	4, 4, 8	600, 600, 300
2010 Mar 10	265.53	+12.9	VLT	XSHOOTER	UV+VIS+NIR	3150–24790	0.8, 0.8, 3.2	4, 4, 8	600, 600, 300
2010 Mar 12	267.55	+14.9	SOAR	GOODMAN	RALC300	3556–8884	0.8, 0.8, 3.2	3	600
2010 Mar 13	268.55	+15.9	VLT	XSHOOTER	UV+VIS+NIR	3150–24790	0.8, 0.8, 3.2	4, 4, 8	600, 600, 300
2010 Mar 15	270.54	+17.9	VLT	XSHOOTER	UV+VIS+NIR	3150–24790	0.8, 0.8, 3.2	4, 4, 8	600, 600, 300
2010 Mar 15	270.74	+18.1	DUP	WFCCD	B	3674–9254	7	3	600
2010 Mar 20	275.66	+23.0	DUP	WFCCD	B	3674–9252	7	1	900
2010 Apr 17	304.50	+51.9	GEM-S	GMOS	B600	3582–6420	8	1	2500
2010 Apr 22	309.50	+56.9	GEM-S	GMOS	R400	5378–9636	8	1	2500
2010 Nov 04	504.81	+252.2	VLT	FORS2	300V	3150–8883	9	1	1793

^aDays since B_{max} (JD−2455252.65).

Table 5. Lightcurve Parameters of SNe 2008ha and 2010ae.

Filter	Peak Time (JD-2,450,000)	Peak Obs. (mag)	Peak Abs. (mag)	Δm_{15} (mag)
SN 2008ha				
<i>u'</i>	4782.23±1.40	19.33±0.12	-12.64±0.16	2.74±0.31
<i>B</i>	4782.43±1.50	18.13±0.06	-13.79±0.14	2.03±0.20
<i>g'</i>	4783.76±0.22	17.87±0.02	-14.01±0.14	1.80±0.03
<i>V</i>	4785.67±0.48	17.74±0.01	-14.11±0.14	1.29±0.04
<i>r'</i>	4788.15±0.51	17.67±0.01	-15.15±0.14	1.11±0.04
<i>i'</i>	4789.05±0.55	17.74±0.02	-14.04±0.14	0.85±0.04
<i>Y</i>	4790.31±0.79	17.50±0.04	-14.21±0.14	...
<i>J</i>	4791.01±1.27	17.72±0.04	-13.98±0.14	...
<i>H</i>	4792.01±2.41	17.18±0.08	-14.50±0.15	...
SN 2010ae				
<i>B</i>	5252.65±0.20	17.65±0.02	-13.44 $\gtrsim M_B \gtrsim$ -15.47±0.54	2.43±0.11
<i>g'</i>	5253.00±0.18	17.49±0.02	-13.54 $\gtrsim M_g \gtrsim$ -15.33±0.54	1.51±0.05
<i>V</i>	5254.74±0.18	17.17±0.02	-13.80 $\gtrsim M_V \gtrsim$ -15.33±0.54	1.15±0.04
<i>r'</i>	5255.78±0.30	16.92±0.01	-13.99 $\gtrsim M_r \gtrsim$ -15.29±0.54	1.01±0.03
<i>i'</i>	5257.04±0.23	16.82±0.01	-14.01 $\gtrsim M_i \gtrsim$ -14.99±0.54	0.80±0.04
<i>z'</i>	5257.70±0.31	16.58±0.02	-14.18 $\gtrsim M_z \gtrsim$ -14.88±0.54	0.76±0.04
<i>Y</i>	5261.47±0.72	16.07±0.02	-14.64 $\gtrsim M_Y \gtrsim$ -15.16±0.54	...
<i>J</i>	5258.75±0.53	16.13±0.05	-14.56 $\gtrsim M_J \gtrsim$ -14.99±0.54	0.74±0.03
<i>H</i>	5260.97±0.80	15.66±0.02	-14.99 $\gtrsim M_H \gtrsim$ -15.26±0.54	0.77±0.07

Appendix A: Supernova 2008ha

SN 2008ha was discovered in the irregular galaxy UGC 12682 on 2008 November 7.17 UT through the course of the Puckett Observatory Supernova Search (Puckett et al. 2010). With J2000.0 coordinates of $\alpha = 23^{\text{h}}34^{\text{m}}52^{\text{s}}.69$ and $\delta = +18^{\circ}13'35''.4$, the SN was positioned approximately $12''$ West and $0''.5$ South from the center of its host. According to NED, the Schlafly & Finkbeiner (2011) recalibration of the Schlegel, Finkbeiner & Davis (1998) dust maps provides a visual extinction value $A_V = 0.21$ mag. This value is adopted in our analysis, and is slightly lower than the Schlegel dust maps value (adopted by Valenti et al. 2009 and Foley et al. 2009) of $A_V = 0.25$ mag. To set the absolute flux scale of SN 2008ha the NED Virgo Infall corrected redshift distance of 1553 ± 17 km s $^{-1}$ is adopted, which for an $H_0 = 73 \pm 5$ km s $^{-1}$ Mpc $^{-1}$, corresponds to 21.3 ± 1.5 Mpc or $\mu = 31.64 \pm 0.15$ mag.

Optical ($u'g'r'i'$) and NIR (YJH) imaging of SN 2008ha was obtained at the Las Campanas Observatory using facilities available to the *Carnegie Supernova Project*. Depending on the particular filter as many as 18 epochs of optical imaging was obtained with the Swope telescope covering the flux evolution from approximately -1 d to $+28$ d relative to $T(B)_{max}$. Our NIR follow up was considerably more sparse consisting of five epochs of imaging with the Swope (+RetroCam) ranging from $+0.2$ d to $+18.1$ d relative to $T(B)_{max}$. The data were processed in the standard manner, including template subtraction, following the methods described in Contreras et al. (2010) and Stritzinger et al. (2011).

Differential PSF photometry of the SN was computed from template subtracted science images relative to a local sequence of stars calibrated over the course of multiple photometric nights with respect to the Landolt (1992), Persson et al. (1998), and Smith et al. (2002) standard fields. Coordinates and final magnitudes of the local sequence are provided in Table A.1. Definitive optical and NIR photometry of SN 2008ha in the standard photometric systems are given in Table A.2 and Table A.3, respectively.

Table A.1. Optical and NIR photometry of the local sequence of SN 2008ha in the standard system.

STAR	α (2000)	δ (2000)	u' (mag)	g' (mag)	r' (mag)	i' (mag)	B (mag)	V (mag)	Y (mag)	J (mag)	H (mag)
01	23 ^h 34 ^m 35 ^s .95	+18° 12' 38".84	18.929(026)	16.912(011)	16.230(011)	16.017(011)	17.399(018)	16.515(010)
02	23 ^h 35 ^m 03 ^s .38	+18° 16' 33".89	17.072(040)	15.163(012)	14.431(018)	14.166(011)	15.672(020)	14.732(010)	13.441(104)	13.133(045)	12.711(069)
03	23 ^h 34 ^m 53 ^s .76	+18° 10' 46".81	15.778(021)	14.734(008)	...	13.042(009)	12.843(012)	12.522(011)
04	23 ^h 34 ^m 47 ^s .41	+18° 17' 39".86	17.098(071)	15.147(016)	...	12.195(008)	11.884(016)	11.307(020)
05	23 ^h 34 ^m 43 ^s .55	+18° 12' 38".84	19.099(082)	16.173(009)	14.832(008)	14.189(010)	16.876(008)	15.457(019)	13.060(010)	12.688(014)	12.059(008)
06	23 ^h 34 ^m 37 ^s .55	+18° 10' 31".82	17.076(024)	15.633(007)	15.071(007)	14.861(008)	16.047(008)	15.294(007)
07	23 ^h 34 ^m 55 ^s .68	+18° 16' 25".85	18.030(030)	15.873(007)	15.114(007)	14.857(008)	16.388(008)	15.443(009)	14.050(009)	13.800(010)	13.355(017)
08	23 ^h 34 ^m 43 ^s .29	+18° 14' 52".89	17.034(018)	15.788(007)	15.277(007)	15.068(008)	16.174(008)	15.484(007)	14.326(010)	14.110(023)	13.776(025)
09	23 ^h 34 ^m 45 ^s .84	+18° 10' 45".86	18.854(033)	16.378(007)	15.431(007)	15.083(008)	16.952(008)	15.869(007)	14.182(009)	13.845(010)	13.275(010)
10	23 ^h 34 ^m 58 ^s .98	+18° 15' 59".85	20.017(054)	16.912(008)	15.513(009)	14.781(009)	17.661(011)	16.160(014)	13.605(008)	13.222(015)	12.559(020)
11	23 ^h 35 ^m 01 ^s .21	+18° 10' 10".80	18.653(051)	16.402(007)	15.624(007)	15.345(008)	16.936(008)	15.954(007)	14.505(010)	14.203(018)	13.738(017)
12	23 ^h 34 ^m 36 ^s .90	+18° 17' 07".84	18.444(031)	16.576(007)	15.842(007)	15.555(008)	17.067(008)	16.159(009)
13	23 ^h 34 ^m 52 ^s .61	+18° 13' 22".83	17.971(020)	16.666(008)	16.179(007)	16.003(008)	17.053(008)	16.378(007)
14	23 ^h 34 ^m 41 ^s .30	+18° 10' 57".85	17.974(016)	16.851(021)	16.402(008)	16.230(008)	17.203(012)	16.586(010)
15	23 ^h 34 ^m 55 ^s .05	+18° 17' 04".89	18.398(030)	16.967(008)	16.431(007)	16.241(008)	17.367(011)	16.643(012)	15.530(008)	15.307(014)	14.967(011)
16	23 ^h 34 ^m 36 ^s .86	+18° 11' 23".86	20.478(066)	17.672(009)	16.646(007)	16.280(008)	18.276(012)	17.117(007)
17	23 ^h 34 ^m 47 ^s .99	+18° 11' 00".86	19.158(049)	17.430(009)	16.774(007)	16.536(008)	17.888(010)	17.047(009)	15.757(010)	15.457(019)	15.053(018)
18	23 ^h 34 ^m 52 ^s .89	+18° 11' 09".89	18.686(027)	17.418(008)	16.962(007)	16.805(008)	17.782(009)	17.139(007)	16.134(008)	15.878(015)	15.556(017)
19	23 ^h 34 ^m 45 ^s .73	+18° 16' 17".88	18.974(027)	17.525(008)	16.955(010)	16.742(008)	17.948(012)	17.196(011)
20	23 ^h 35 ^m 07 ^s .11	+18° 17' 56".84	18.749(057)	17.498(030)	16.945(014)	16.760(016)	17.855(026)	17.144(014)
21	23 ^h 34 ^m 38 ^s .28	+18° 12' 28".87	19.757(119)	17.834(009)	17.082(007)	16.781(008)	18.363(012)	17.384(019)
22	23 ^h 34 ^m 49 ^s .31	+18° 14' 23".80	19.652(055)	18.409(010)	17.071(007)	16.483(014)	19.103(038)	17.714(010)	15.386(012)	14.988(012)	14.373(009)
23	23 ^h 34 ^m 59 ^s .47	+18° 13' 27".88	...	18.270(009)	17.214(007)	16.832(009)	18.902(016)	17.713(012)	15.916(007)	15.552(018)	14.961(012)
24	23 ^h 35 ^m 08 ^s .38	+18° 15' 26".88	...	18.628(009)	17.265(010)	15.957(016)	19.464(026)	17.862(016)	14.441(007)	14.007(009)	13.408(009)
25	23 ^h 34 ^m 39 ^s .18	+18° 14' 36".85	...	18.756(009)	17.400(014)	16.433(015)	19.569(027)	18.034(026)	15.153(016)	14.735(014)	14.106(008)
26	23 ^h 35 ^m 08 ^s .00	+18° 12' 44".81	...	18.827(009)	17.836(008)	17.455(013)	19.386(024)	18.283(017)
27	23 ^h 34 ^m 55 ^s .17	+18° 18' 43".84	...	18.882(009)	17.772(008)	17.307(009)	19.505(027)	18.278(035)
28	23 ^h 35 ^m 16 ^s .19	+18° 18' 00".86	13.175(008)	12.935(025)	12.554(015)
29	23 ^h 35 ^m 13 ^s .81	+18° 11' 39".82	14.059(010)	13.806(021)	13.405(010)
30	23 ^h 34 ^m 49 ^s .67	+18° 18' 54".81	14.337(007)	14.035(015)	13.564(011)
31	23 ^h 34 ^m 43 ^s .52	+18° 19' 09".90	14.303(009)	14.055(019)	13.665(021)
32	23 ^h 35 ^m 13 ^s .13	+18° 12' 05".88	14.994(017)	14.772(034)	14.447(012)
33	23 ^h 35 ^m 01 ^s .45	+18° 09' 36".89	15.717(011)	15.211(012)	14.536(014)
34	23 ^h 34 ^m 44 ^s .67	+18° 08' 57".81	15.882(012)	15.367(028)	14.866(027)
35	23 ^h 35 ^m 09 ^s .00	+18° 18' 03".84	15.908(014)	15.423(032)	14.914(048)
36	23 ^h 35 ^m 12 ^s .94	+18° 19' 15".89	16.116(016)	15.714(024)	15.096(012)
37	16.304(012)	15.811(020)	15.323(023)

Note. — Uncertainties given in parentheses in thousandths of a magnitude correspond to an rms of the magnitudes obtained on photometric nights.

Table A.2. Swope optical photometry of SN 2008ha in the standard system.

JD-2,454,000+	u' (mag)	g' (mag)	r' (mag)	i' (mag)	B (mag)	V (mag)
781.6	19.332(138)	17.992(041)	18.004(044)	18.104(044)	18.144(049)	17.911(035)
783.6	19.390(131)	17.853(032)	17.868(028)	17.963(033)	18.154(054)	17.771(036)
785.6	19.644(098)	17.936(018)	17.701(019)	17.799(023)	18.294(039)	17.746(020)
786.5	19.922(061)	18.027(015)	17.709(015)	17.800(015)	18.393(020)	17.738(016)
789.6	20.574(080)	18.352(016)	17.692(020)	17.730(028)	18.878(030)	17.918(020)
792.5	21.181(125)	18.717(106)	17.861(031)	17.814(044)	19.447(045)	18.208(028)
793.5	21.235(146)	19.048(144)	18.009(075)	17.950(042)	19.612(061)	18.344(027)
795.5	21.623(188)	19.247(127)	18.242(035)	18.136(034)	19.977(073)	18.600(041)
797.5	22.207(335)	19.571(029)	18.425(022)	18.243(025)	20.244(203)	18.849(168)
798.5	22.482(395)	19.637(029)	18.476(023)	18.317(033)	20.147(145)	18.848(096)
801.6	22.591(357)	19.822(035)	18.694(028)	18.476(036)	20.490(085)	19.043(046)
802.5	...	19.935(266)	18.738(064)	18.521(056)	20.538(071)	19.136(034)
803.5	...	19.907(037)	18.813(031)	18.565(034)	20.722(178)	19.118(085)
806.5	...	20.308(262)	18.952(058)	18.695(064)	...	19.301(064)
807.5	...	20.174(357)	19.092(113)	18.715(083)	...	19.286(091)
808.5	19.150(108)	18.987(120)	...	19.498(136)
809.5	...	20.491(387)	19.272(075)	18.915(095)	...	19.593(116)
810.5	19.250(080)	18.956(087)	...	19.509(096)

Note. — Values in parentheses are 1σ measurement uncertainties in millimag.

Table A.3. Swope NIR photometry of SN 2008ha in the standard system.

JD-2, 454, 000+	<i>Y</i> (mag)	<i>J</i> (mag)	<i>H</i> (mag)
782.6	17.832(096)	17.819(438)	17.652(115)
784.6	17.872(090)	17.768(058)	17.468(130)
787.6	17.540(021)	17.663(046)	17.281(072)
791.5	17.504(030)	17.674(062)	...
800.5	17.945(045)	17.824(116)	17.552(121)

Note. — Values in parentheses are 1σ measurement uncertainties in millimag.